Modelling and Analysis of Wirelessly Interrogated SAW based Micropumps for Drug Delivery Applications

by

Don Wenura Eranda Dissanayake

B. Eng Computer Systems (First Class Honours),
University of Adelaide, 2004

Thesis submitted for the degree of

Doctor of Philosophy

in

School of Electrical and Electronic Engineering,
Faculty of Engineering, Computer and Mathematical Sciences
The University of Adelaide

April 2010

Chapter 5

Diffuser Design and Analysis

IN valveless diffuser micropumps, diffuser elements are used as flow directing elements. In a diffuser element, the difference in the flow resistances in the diffuser and nozzle directions, cause the flow rectification.

In this Chapter, the important functionality played by diffuser elements in valveless micropumps are investigated. Computational Fluid Dynamics (CFD) based flow characteristics of diffuser elements are analysed and presented. Moreover, microfluidic flow characteristics of low Reynolds number laminar flow through gradually expanding flat–walled diffusers are investigated, in view of their applications in low–powered microfluidic devices. A detailed theoretical analysis of diffuser elements, and the relationship between the dimensions and the performance of these elements are presented and discussed. ANSYS based FEM and FEA results are discussed to highlight the importance in parameter optimisation.

The results from the numerical analysis were quantified in terms of pressure loss coefficient. The pressure loss coefficients were used to calculate the diffuser efficiency for 3D diffuser elements. Contrary to past claims, flow rectification is shown to be indeed possible for laminar flows.

5.1 Introduction

In order to obtain flow rectification from the oscillatory motion of the diaphragm, valves are incorporated into the design of diaphragm based micropumps. As was discussed in Chapter 2, static fixed–geometry microvalves consist of host of advantages over dynamic valves. As such; the absence of moving parts, and elimination of wear and fatigue issues are highly regarded. Moreover, out of fixed–geometry microvalves, diffuser elements performs a major role in valveless micropump design. Such diffusers are used in valveless micropumps to cause flow rectification, and thus lead to pumping action in one preferential direction. Therefore, diffuser elements were chosen as the flow directing valves for the proposed micropump structure.

5.1.1 Diffuser Elements for Valveless Flow Rectification

Based on the comprehensive review carried out in Chapter 2, diffuser elements can be identified as easy to implement, yet effective technique for valveless flow rectification of micropumps. Generally, valveless micropumps are considered very attractive as they are low cost devices due to their simple structure. Interestingly, different diffuser geometries such as conical, pyramidal and flat-walled diffusers have been widely used for valveless micropumps (Wang *et al.* 2008, Singhal *et al.* 2004, Olsson *et al.* 2000). The choice of diffuser shape is basically dependent on the fabrication process. For planar lithography and standard micromachining fabrication techniques, flat-walled diffusers (planar diffusers) are considered to be the best choice (Wang *et al.* 2008). The planar configuration of these flat-walled diffusers widens the spectrum of possible materials and pump driver designs. Moreover, the increasing use of polymer materials are foreseeable because of their potential low cost and good biocompatibility and chemical resistance. Another potential advantage of the flat-walled diffuser is that, under the same inlet boundary-layer condition, the best flat-walled diffuser is comparatively shorter than the best conical design, which helps to reduce the device dimensions. Therefore, in designs where the available space is a critical design parameter, the flat-walled diffuser can be used for better performance (Wang *et al.* 2008).

5.1.2 Valveless Diffuser Micropumps

The proposed micropump uses two diffuser/nozzle elements that are connected through a pumping chamber, which consists of an electrostatically actuated conductive diaphragm. When actuated, the diaphragm periodically increases and decreases the volume of the pumping chamber. By changing the orientation of the diffuser elements such that the wide end of one is attached to the chamber on one side and the narrow end of the other is attached to the opposite side, a net pumping action across the chamber occurs (Figure 5.1) as the diaphragm vibrates up and down at a predefined frequency.

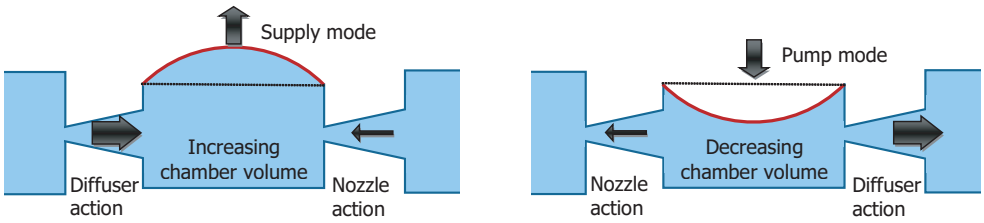

Figure 5.1. Valveless diffuser micropump model. Illustration of the flow rectification phenomena in a valveless/diffuser micropump while the micropump is in supply mode (expansion mode) and pump mode (contraction mode). Here, thicker arrows imply a higher volume flow rate. During supply mode, more fluid flow into the chamber through inlet than the outlet and during pump mode, more fluid flow out from the outlet than the inlet. This behaviour results in a net fluid flow from the inlet to the outlet.

Organisation of this chapter is as follows. Section 5.2 presents a detailed theoretical analysis of diffuser elements, considering various performance indicators such as diffuser efficiency, flow rectification efficiency of diffusers. In addition, Section 5.2 also provides a dimensional analysis of diffusers, in order to optimise diffuser parameters. Then in Section 5.3, CFD based numerical analysis of diffuser elements are presented. Moreover, Section 5.3 provides a detailed analysis of diffuser performance for low Reynolds numbers, and then followed by a summary in Section 5.4.

5.2 Theoretical Analysis of Diffusers

By definition, a diffuser element is a device for reducing the velocity and increasing the static pressure of a fluid passing through a system (Olsson *et al.* 2000). In view of

the ease of integrating with other MEMS devices, flat-walled (planar) diffuser/nozzle elements can be employed, which has the features of square cross-section, two parallel flat walls, and two convergent flat walls. The schematic diagram (top view) of the diffuser/nozzle element is shown in Figure 5.2. The main geometrical parameters of the diffuser/nozzle element are; the diverging diffuser angle 2θ, the diffuser length L and the neck width $W1$. The flow rectification ability of the valveless micropump depends on the difference between the pressure loss in the diffuser and the nozzle directions (Cui *et al.* 2008), which is presented in detail in coming sections.

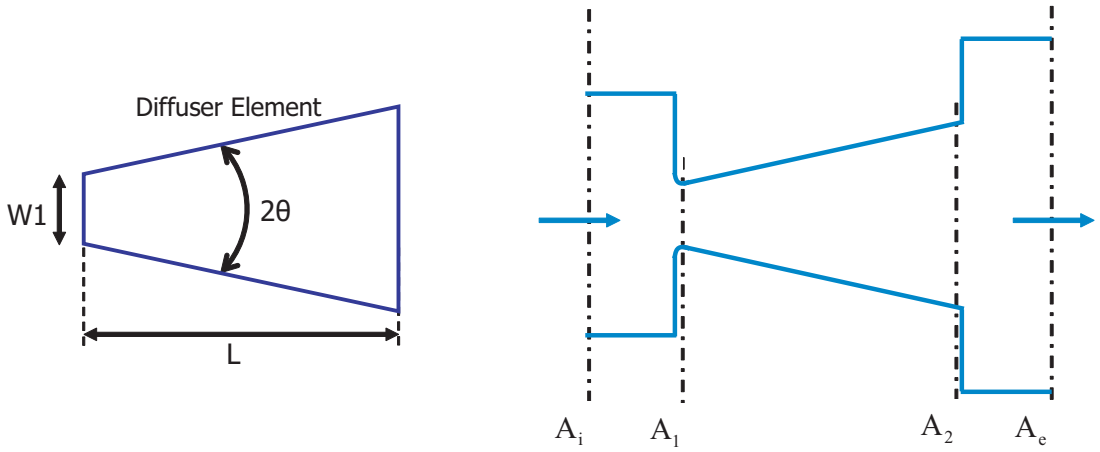

Figure 5.2. Flat–walled diffuser element. LEFT: Top view of a flat–walled diffuser element and diffuser design parameters. Main geometrical parameters of the diffuser/nozzle element involve the diverging diffuser angle 2θ, the diffuser length L and the neck width $W1$. RIGHT: Top view of a flat–walled diffuser, which is connected to an inlet duct and an outlet duct. The arrows indicate the diffuser direction $(i - e)$, and the nozzle direction is from $e - i$.

In the literature, several steady–flow measurements on flat–walled diffusers for micropump applications have been reported (Wang *et al.* 2008). However, the experimental data are hard to be used to optimise the diffuser design for the following reasons;

(i) The range of the diverging angles of the tested diffusers is very limited; the selection of the tested angles was based on the results of high Reynolds number flows and, therefore, was almost in a range of small values,

(ii) The slenderness and the inlet aspect ratio of the reported diffusers are very scattered. Additionally, it has been shown that both parameters have prominent effects on the performance of the diffuser micropump (Wang *et al.* 2008, Cui *et al.* 2008, Olsson *et al.* 2000).

(iii) In most experiments, the reported pressure loss was not contributed only by the diffuser but also by other components (such as inlet and outlet channels, sudden expansion and contraction, bends) which were not clearly described. Therefore, the reported data represent the total pressure loss of all the components instead of the pressure loss due to the diffuser valve solely (Wang *et al.* 2008).

Due to these reasons it is important to follow a consistent design approach to analyse the diffuser elements to prevent any misinterpretation of results and findings.

5.2.1 Pressure Loss Coefficient

It is known that the performance of a valveless micropump depends on the properties of the diffuser/nozzle elements. Hence it is important to analyse the effect of diffuser geometry during the dynamic operation of the designed micropump. Figure 5.2 shows a top view of flat–walled diffuser, which is connected to an inlet and outlet ducts with cross–sectional areas A_i and A_e respectively. Subscripts i and e denote the inlet duct and outlet duct locations as shown in Figure 5.2. The inlet and outlet areas of the diffuser are denoted by A_1 and A_2, respectively. For an incompressible flow through the diffuser, the energy equation per unit volume of fluid between the inlet and outlet ducts' cross–sectional planes can be expressed as

$$p_i + \frac{1}{2}\alpha_i \rho_L \overline{v}_i{}^2 = p_e + \frac{1}{2}\alpha_e \rho_L \overline{v}_e{}^2 + \Delta p_{i-e}, \tag{5.1}$$

where p is the hydrostatic pressure across the cross–section, ρ_L is the incompressible fluid density. The volume–averaged velocity $\overline{v}$ is defined as (White 1999)

$$\overline{v} = \frac{1}{A}\int_A u_a \, dA, \tag{5.2}$$

for axial velocity u_a across the cross–section. As the flow entering or leaving a cross–section is multidimensional, the kinetic–energy correction factor α is considered in Equation 5.1 and defined as (Wang *et al.* 2008)

$$\alpha = \frac{1}{\overline{v}^3 A}\int_A u_a{}^3 \, dA. \tag{5.3}$$

Here α is 2 for fully–developed laminar flow in a circular or square tube, and α is close to unity for turbulent flow (White 1999). Moreover Δp_{i-e} in Equation 5.1 is the total pressure loss across the segment $i-e$ due to irreversible viscus dissipation. Alternatively, the total pressure loss across the diffuser element can be considered as the sum of the pressure drops through the three parts; (i) the sudden contractions at the entrance (Δp_{i-1}), (ii) the sudden expansions at the exit (Δp_{2-e}), and (iii) the gradual expansions or contractions along the length of the diffuser element (Δp_{1-2}). Therefore,

$$\Delta p_{i-e} = \Delta p_{i-1} + \Delta p_{1-2} + \Delta p_{2-e}. \tag{5.4}$$

In classical fluid dynamics, the pressure loss coefficient for a diffuser element (from cross–sections 1–2) is often defined as

$$K_{1-2} = \frac{\Delta p_{1-2}}{\frac{1}{2}\rho_L [max(\overline{v}_1, \overline{v}_2)]^2}, \tag{5.5}$$

where Δp_{1-2} is the pressure drop across the diffuser direction, and $\overline{v}_1$ and $\overline{v}_2$ are volume–averaged velocities as defined in Equation 5.2.

However, based on three dimensional continuity of mass for an incompressible fluid flow in a diffuser–duct combination, the fluid flow rate is, $Q = A_1\overline{v}_1 = A_2\overline{v}_2$ (White 1999). Therefore the maximum volume–averaged velocity can be observed at the diffuser neck (across A_1). Consequently, the total pressure loss coefficient of the diffuser-duct combination in diffuser direction can be written as

$$K_{i-e} = \frac{\Delta p_{i-e}}{\frac{1}{2}\rho_L \overline{v}_1{}^2}. \tag{5.6}$$

Hence, using Equations 5.4 and 5.6, total pressure loss coefficient across the diffuser direction (K_d) can be written as (Wang *et al.* 2008, Tsui and Lu 2008)

$$\begin{aligned} K_d &= K_{i-e} = K_{i-1} + K_{1-2} + K_{2-e}\left(\frac{A_1}{A_2}\right)^2, \\ &= \frac{p_i - p_e}{\frac{1}{2}\rho_L \overline{v}_1{}^2} + \alpha_{d,i}\left(\frac{A_1}{A_i}\right)^2 - \alpha_{d,e}\left(\frac{A_1}{A_e}\right)^2. \end{aligned} \tag{5.7}$$

By following a similar approach, the total pressure loss coefficient across the nozzle direction (K_n) can be written as (Wang *et al.* 2008, Tsui and Lu 2008)

$$\begin{aligned} K_n &= K_{e-i} = K_{1-i} + K_{2-1} + K_{e-2}\left(\frac{A_1}{A_2}\right)^2, \\ &= \frac{p_e - p_i}{\frac{1}{2}\rho_L \overline{v}_1{}^2} + \alpha_{n,e}\left(\frac{A_1}{A_e}\right)^2 - \alpha_{n,i}\left(\frac{A_1}{A_i}\right)^2. \end{aligned} \tag{5.8}$$

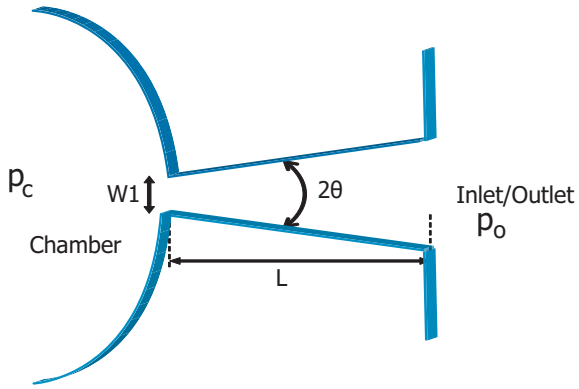

Figure 5.3. Schematic of a diffuser valve. Here the diffuser is connected directly to a large pumping chamber and an inlet or outlet port. Pressure in the chamber is p_c and in the inlet/outlet is p_o.

As can be seen in Figure 5.3, generally in valveless diffuser micropumps the diffuser is connected directly to a large pumping chamber and either an inlet or outlet port. This is corresponding to situations of thin inlet boundary layer at A_1 and a free discharge at A_2. Therefore in such a diffuser–chamber combination, the total pressure loss coefficients can be simplified as $A_i \gg A_1$ and $A_e \gg A_2$. As a result Equations 5.7 and 5.8 can be simplified and rewritten as follows.

$$K_d = K_{d,en} + K_{d,l} + K_{d,ex}\left(\frac{A_1}{A_2}\right)^2 \approx \frac{p_c - p_o}{\frac{1}{2}\rho_L \overline{v}_1{}^2}, \tag{5.9}$$

$$K_n = K_{n,ex} + K_{n,l} + K_{n,en}\left(\frac{A_1}{A_2}\right)^2 \approx \frac{p_o - p_c}{\frac{1}{2}\rho_L \overline{v}_1{}^2}. \tag{5.10}$$

Here $K_{d,en} = K_{i-1}$, $K_{d,l} = K_{1-2}$ and $K_{d,ex} = K_{2-e}$. Similarly, $K_{n,en} = K_{e-2}$, $K_{n,l} = K_{2-1}$ and $K_{n,ex} = K_{1-i}$. p_o and p_c are hydrostatic pressures in the inlet/outlet and the chamber respectively, as shown in Figure 5.3. Furthermore, these loss coefficient components in Equations 5.9 and 5.10 can be rewritten by considering the above simplifications together with Equations 5.1 and 5.5.

$$K_{d,en} \approx \frac{p_c - p_1}{\frac{1}{2}\rho_L \overline{v}_1{}^2} - \alpha_{d,1}, \quad K_{n,en} \approx \frac{p_o - p_2}{\frac{1}{2}\rho_L \overline{v}_2{}^2} - \alpha_{n,2}, \tag{5.11}$$

$$K_{d,ex} \approx \frac{p_2 - p_o}{\frac{1}{2}\rho_L \overline{v}_2{}^2} - \alpha_{d,2}, \quad K_{n,ex} \approx \frac{p_1 - p_c}{\frac{1}{2}\rho_L \overline{v}_1{}^2} - \alpha_{n,1}, \tag{5.12}$$

$$K_{d,l} = \frac{p_1 - p_2}{\frac{1}{2}\rho_L \overline{v}_1{}^2} + \alpha_{d,1} - \alpha_{d,2}\left(\frac{A_1}{A_2}\right)^2, \tag{5.13}$$

$$K_{n,l} = \frac{p_2 - p_1}{\frac{1}{2}\rho_L \overline{v}_1{}^2} + \alpha_{n,2}\left(\frac{A_1}{A_2}\right)^2 - \alpha_{n,1}. \tag{5.14}$$

5.2.2 Diffuser Efficiency

The diffuser efficiency; the efficiency of diffuser/nozzle elements is commonly defined as the ratio of the pressure loss coefficient across the nozzle direction to that in the diffuser direction;

$$\eta = \frac{K_n}{K_d}. \tag{5.15}$$

If the pressure loss coefficient in the nozzle direction is higher than that in the diffuser direction, that is if $\eta > 1$, a pumping action from the inlet to the outlet is caused (Wang *et al.* 2008, Singhal *et al.* 2004, Olsson *et al.* 2000). In contrast, $\eta < 1$ will lead to a pumping action from the outlet to the inlet (inverted). The case where $\eta = 1$ corresponds to equal pressure drops in both the nozzle and the diffuser directions, leading to no flow rectification (Wang *et al.* 2008, Singhal *et al.* 2004). Therefore some care is needed while designing the diffuser elements in order to achieve the expected outcomes.

5.2.3 Flow Rectification Efficiency

The flow rectification efficiency of a valveless micropump is a measure of the ability of the pump to direct the flow in one preferential direction. Once the total pressure loss coefficients are known for diffuser/nozzle elements, using the continuity theory, the flows across diffuser and nozzle directions, Q_d and Q_n are respectively expressed as

$$Q_d = A_1 \left(\frac{2}{\rho_L}\right)^{1/2} \left(\frac{p_c - p_o}{K_d}\right)^{1/2}, \tag{5.16}$$

$$Q_n = A_1 \left(\frac{2}{\rho_L}\right)^{1/2} \left(\frac{p_o - p_c}{K_n}\right)^{1/2}. \tag{5.17}$$

During the supply mode of the micropump, the chamber volume increases thus resulting in a net flow into the pump chamber. In this mode, the inlet element acts as the diffuser and the outlet element acts as the nozzle. Therefore the flow in the forward direction is given by $Q_+ = Q_d$ and in backward direction by $Q_- = Q_n$. During the pump mode, the chamber volume decreases, thus resulting in net flow out of the chamber with the inlet element acting as the nozzle and the outlet element acting as the diffuser. Here the flow in the forward direction is given by $Q_+ = Q_n$ and in backward direction by $Q_- = Q_d$. As a result, the flow rectification efficiency of the valveless micropump can be expressed as (Singhal *et al.* 2004)

$$\eta_{rec} = \frac{Q_+ - Q_-}{Q_+ + Q_-}. \tag{5.18}$$

A higher η_{rec} corresponds to a better flow rectification. In particular, for perfect rectification, flow is only in one direction and $\eta_{rec} = 1$, while when there is no flow rectification, equal amounts of fluid move in both directions and $\eta_{rec} = 0$.

As it can be seen from Equations 5.15 – 5.18, the flow rectification efficiency of a valveless micropump is related to the diffuser efficiency of the nozzle–diffuser elements. As the difference between K_n and K_d increases, η_{rec} for the micropump also increases. Based on these analysis, it is evident that the flow rectification effect of the device depends on the diffuser geometry and is further analysed in the next section, considering dimensional parameters.

5.2.4 Dimensional Analysis of Diffusers

In order to analyse the dependency of diffuser performance on its dimensions, pressure recovery coefficient C_p is commonly used in practice (Olsson 1998, White 1999, Singhal *et al.* 2004). Pressure recovery coefficient is defined as

$$C_p = \frac{p_2 - p_1}{\frac{1}{2}\rho_L \overline{v}_1{}^2}, \tag{5.19}$$

where p_1, p_2, ρ_L and $\overline{v}_1$ are as defined before in Section 5.2.1. By combining Equations 5.13 and 5.19, an alternative expression for pressure loss coefficient can be written as

$$K_{d,l} = \alpha_{d,1} - \alpha_{d,2}\left(\frac{A_1}{A_2}\right)^2 - C_p. \tag{5.20}$$

It can be noted that the higher the pressure recovery, lower the diffuser loss; hence a better micropump performance.

Based on the stability map of diffuser flow pattern shown in Figure 5.4, four different regions of flow operation can be identified. These regions depend on the diffuser parameters, θ, L and $W1$. In the *no stall* region (below *aa*), the flow is steady viscous with no separation at the diffuser walls and with moderately good performance (Olsson *et al.* 2000). In the *transitory steady stall* region (between *aa* and *bb*), the flow is unsteady and the maximum pressure recovery C_p is realised. As a result, the pressure loss coefficient is at a minimum in this region, and diffuser performs at its best. In the *bistable steady region* (between *bb* and *cc*), a steady bistable stall can flip–flop from one part of the diffuser wall to another and performance is poor. In the *jet flow* region (above *cc*), the performance extremely poor as the flow separates almost

completely from diffuser walls and passes through the diffuser at a nearly constant cross–sectional.

(a) (b)

Figure 5.4. Stability map of a flat–walled diffuser. (a) 3D geometry of a flat–walled diffuser element. (b) Flat–walled diffuser stability map. Diffuser operates in four different regions depending on the diffuser geometry. Stability map can be used to design a diffuser with a minimal pressure loss coefficient, which is shown as a dashed line in the transitory stall region (White 1999).

Figure 5.5 depicts a typical performance map of a diffuser, where the performance variation based on dimensional parameters such as slenderness ($L/W1$), and area ratio AR ($= A_1/A_2$). As is evident from this graph, the highest C_p, hence the lowest diffuser loss coefficient $K_{d,l}$, is achieved approximately for $3.5 < AR < 4$, $8^\circ < 2\theta < 12^\circ$, and $14 < L/W1 < 20$.

Additionally, dimensional analysis of a flat–walled diffusers shows that, for incompressible flow, the performance of the diffuser also depends on inlet boundary–layer blockage factor (the ratio of the effective area displaced by the inlet boundary layer to the diffuser inlet area). As can be seen form Figure 5.6 (a), generally the performance decreases with the blockage and for both conical and flat-walled diffusers. The boundary–layer blockage factor at the entrance (A_i) depends on the relative length

NOTE:
This figure is included on page 125
of the print copy of the thesis held in
the University of Adelaide Library.

Figure 5.5. Performance map for a flat-walled diffuser. The AR is defined as the area ratio between exit and throat. Maximum C_p occurs when $L/W1$ is between 14 – 20, diffuser angle 2θ is between 8 – 12 °, and AR falls between 3.5 – 4 (White 1999).

of the upstream duct and has significant effects on the performance of the diffuser (Wang *et al.* 2008).

Moreover, as can be seen from the Figure 5.6 (b), the entrance geometry plays an important role in minimising pressure loss of a diffuser. Sharp edges at the entrance cause large zones of flow separation and large losses. In contrast, a diffuser with a well rounded entrance has shown negligible pressure loss. However, it was discussed in (Wang *et al.* 2008) that the losses at the exit of a diffuser stays unchanged irrespective of whether the exit well rounded or not.

It has also been shown that the velocity distribution at the diffuser exit (A_e) is always to be non–uniform (White 1999). Furthermore, it is known that the downstream duct provides a settling passage in which the kinetic energy in the distorted outflow is converted to a static pressure rise, due to turbulent mixing (White 1999). Therefore, at high Reynolds numbers, the loss in a diffuser with an outlet duct is smaller than that for the same diffuser with a free discharge. Additionally, the length and the location

of the exit (A_e) should be chosen to achieve a maximum static pressure at the exit P_e (Wang *et al.* 2008).

NOTE:
This figure is included on page 126 of the print copy of the thesis held in the University of Adelaide Library.

(a) (b)

Figure 5.6. Loss coefficients for different inlet/outlet conditions. (a) Sudden expansion and contraction losses. (b) Entrance and exit loss coefficients for rounded and beveled inlets (White 1999).

In the diffuser design, care was taken in defining the distance between A_i and A_1 (also A_2 and A_e) during the FEA by selecting an appropriate ratio between these distances and the diffuser length.

Available information in the literature for macroscopic flow (White 1999, Olsson *et al.* 2000) shows that diffusers with rectangular (flat-walled) and circular (conical) cross-section give about the same maximum performance, but at different divergence angles. However, the best performance for flat-walled diffusers is achieved at a length that is 10 – 80 % less than the best conical diffuser design (White 1999). Consequently, the possibility of using flat–walled diffusers for miniaturised valve-less micropumps makes the design more compact and easy to fabricate due to its symmetrical geometry.

5.3 Numerical Simulations of Diffuser Elements

Computational Fluid Dynamics (CFD) uses numerical methods and algorithms in fluid mechanics, to solve and analyse problems that involve fluid flows. The purpose of carrying out a CFD analysis is to understand how fluid dynamics affects the operation or performance of a device, hardware component or system, from a design and analysis perspective. During CFD analysis, the application of the conservation laws with boundary and initial conditions take place in mathematical discretised form in order to estimate field variables (Huebner *et al.* 2001).

It is been realised that developing analytical models for fluid flow analysis is much more complex compared to the available numerical methods (Löhner 2008). Various researchers have successfully utilised numerical methods to model and analyse the problem of microfluidic flow in MEMS devices (Olsson 1998, Wang *et al.* 2008, Singhal *et al.* 2004, Rosa and Pinho 2006, Gamboa *et al.* 2005). As a result a variety of discretisation methods are available for numerical analysis of fluid dynamics. These include Finite Volume Method (FVM), Finite Element Method (FEM), Finite Difference Method (FDM), and Boundary Element Method (BEM). FEM is found to be much more stable than the FVM approach and subsequently it has become the new direction in which CFD is moving. Additionally the stability and robustness of a solution is considered to be better in FEM, though for some cases it might take more memory than other numerical methods (Huebner *et al.* 2001).

5.3.1 Finite Element Modelling of Flat–walled Diffusers

In FEA, the complex geometry is represented by a mesh that consists of a large number of elements. Therefore, in essence by using FEM, a complex problem can be reduced into a series of greatly simplified problems. Moreover, it consists of variety of ways to formulate the properties of individual elements which is advantages in analysing systems with complex behaviour, such as microfluidic motion in micro–channels and diffuser elements. Due to the aforementioned reasons, industrial software tool ANSYS (ANSYS Incorporation 2009b) based FEM was used for CFD modelling and analysis of flat–walled diffusers. The simulations were first carried out for 2D models and then for 3D models of diffuser elements. Initially, 2D models were designed and analysed to establish an initial validation of simulation methods, to gain confidence on CFD modelling. 2D analysis and results are presented in Section 5.3.2. Then more detailed

and complex 3D modelling was carried out in order to analyse the effects of diffuser parameters and Reynolds number on diffuser performance, which is presented in Section 5.3.3.

5.3.2 2D–CFD Simulations of Flat–walled Diffusers

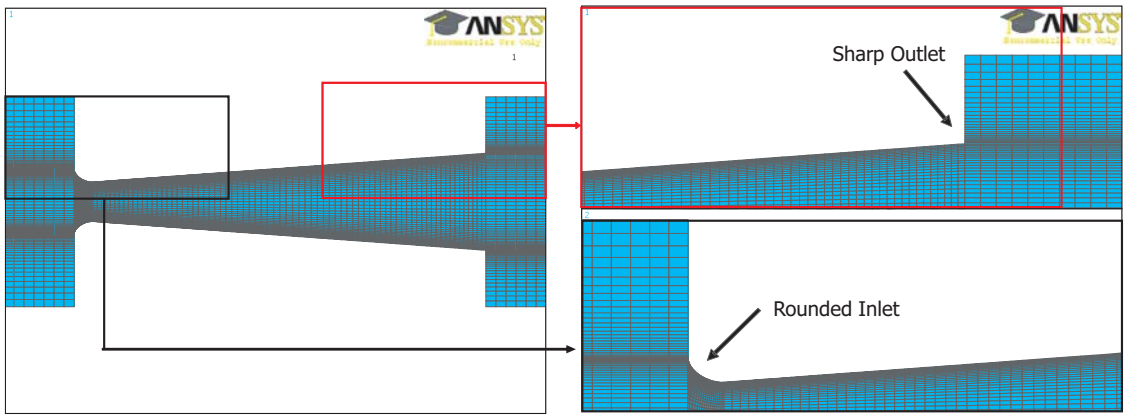

Figure 5.7. Meshed 2D model of a diffuser. Complete meshed model with a rounded inlet and a sharp outlet to minimise pressure losses. Diffuser length $L = 1000$ μm, neck width $W1 = 80$ μm and the diverging angle $2\theta = 10°$.

In order to obtain the optimal design parameters, flat–walled diffusers with different dimensions were designed and simulated by varying the diffuser parameters, 2θ, L and $W1$. A laminar flow analysis was carried out by setting the fluid velocity at the diffuser walls to zero ($Vx = 0$ and $Vy = 0$) to incorporate the no–slip condition at diffuser walls. Considering the values used in the published literature, a pressure gradient (0 – 100 kPa) was set across the diffuser by setting pressure boundary conditions at the inlet and outlet. Properties of water was considered for the fluid filled in the diffusers. As the operation of the micropump is based on a low powered actuation mechanism, and the targeted applications are mainly in nano–liter drug delivery, only low Reynolds number (Re < 1000) based analysis was carried out in this research. ANSYS based 2D simulation results are analysed and, velocity and pressure distributions are depicted in Figure 5.8.

Figure 5.8 shows the resulting contour plots of the velocity and pressure distribution across the diffuser element. The velocity around the inlet is larger compared to the

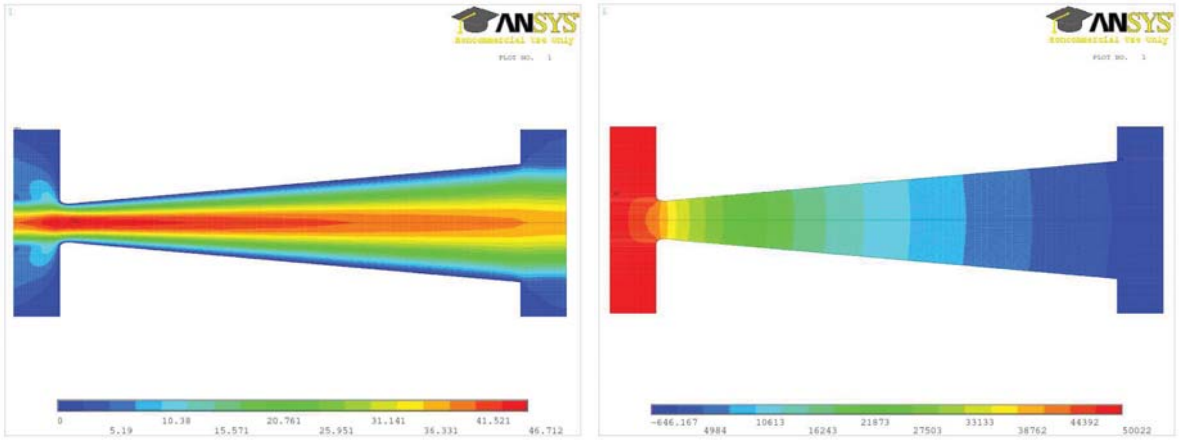

(a) (b)

Figure 5.8. Velocity and pressure distribution of 2D diffuser. (a) Velocity distribution, and (b) Pressure distribution for a two-dimensional model of a flat–walled diffuser element. Diffuser length $L = 1000$ μm, neck width $W1 = 80$ μm and the diverging angle $2\theta = 10^{\circ}$.

other parts of the diffuser and since this depicts the diffuser effect, the pressure is higher around the inlet compared to the exit of the diffuser.

Detailed presentation of the flow behaviour is shown in Figure 5.9, where the vector plots of the velocities for diffuser and nozzle effects are depicted. The velocity across the neck is much higher than that of any other cross–section of the diffuser element. For low Reynolds number laminar flow analysis, flow patterns are proven to be smoother without any flow separation at the exits of the elements.

Based on the 3D plot shown in Figure 5.10 (a), it is apparent that the inlet velocity is larger around the center area of the inlet and also velocity increases as the pressure drop is increased.

The dependency of the inlet velocity in diffuser parameters such as $W1, 2\theta$, and L were also analysed. It should be noted that during the analysis, only one parameter was varied at a time, and other parameters were kept unchanged. The variation in the inlet velocity for different neck widths $W1$ is analysed for different pressure drops and the results are presented in Figure 5.10 (b). According to the analysis, as the neck width is increased, the inlet velocity is also increased for respective pressure drops. Therefore, for higher flow rates, larger neck widths are desired.

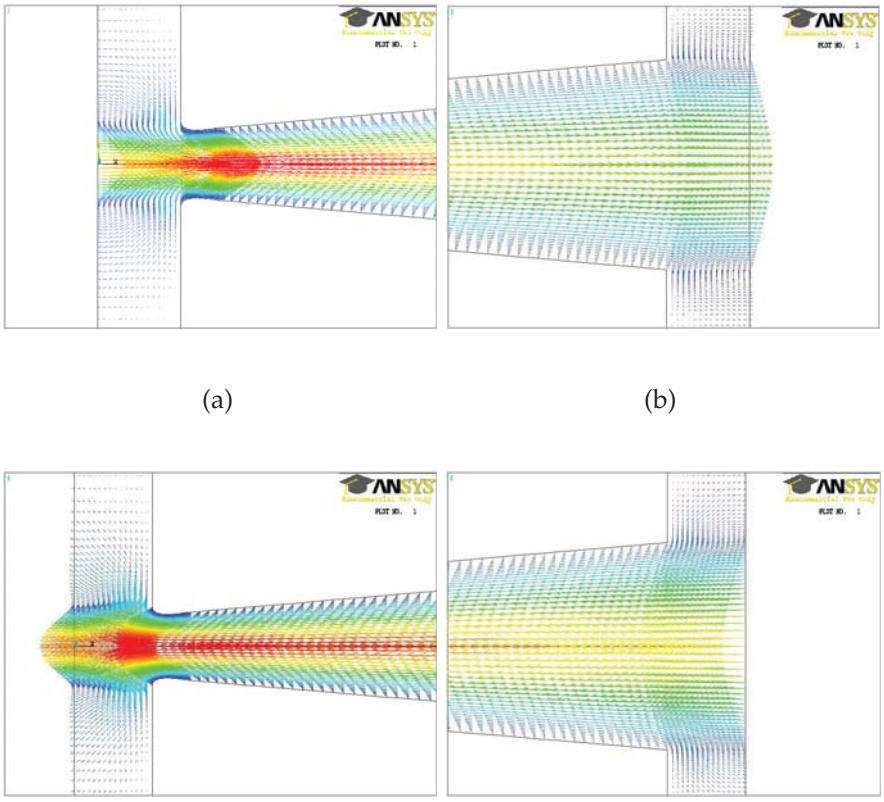

(a) (b)

(c) (d)

Figure 5.9. 2D diffuser vector plots. (a) Vector plot of the velocity at the inlet of the diffuser in diffuser direction (across A_i in Figure 5.2), (b) Vector plot of the velocity at the outlet of the diffuser in diffuser direction (across A_e in Figure 5.2), (c) Vector plot of the velocity at the outlet of the diffuser in nozzle direction (across A_i in Figure 5.2), and (d) Vector plot of the velocity at the inlet of the diffuser in nozzle direction (across A_e in Figure 5.2). The velocity across the neck is much higher than that of any other cross–section of the diffuser element. The laminar flow is realised throughout the diffuser without flow separation for low Reynolds numbers (< 1000).

In order to verify the effect of diverging angle on the flow rate, the variation of the inlet velocity for different diffuser angles 2θ was analysed for different pressure drops and the results are shown in Figure 5.11 (a). Here, as the diffuser angle is increased, the inlet velocity is also increased for respective pressure drops.

Finally, the variation of the inlet velocity for different diffuser lengths L was analysed in ANSYS for different pressure drops and the results are shown in Figure 5.11 (b).

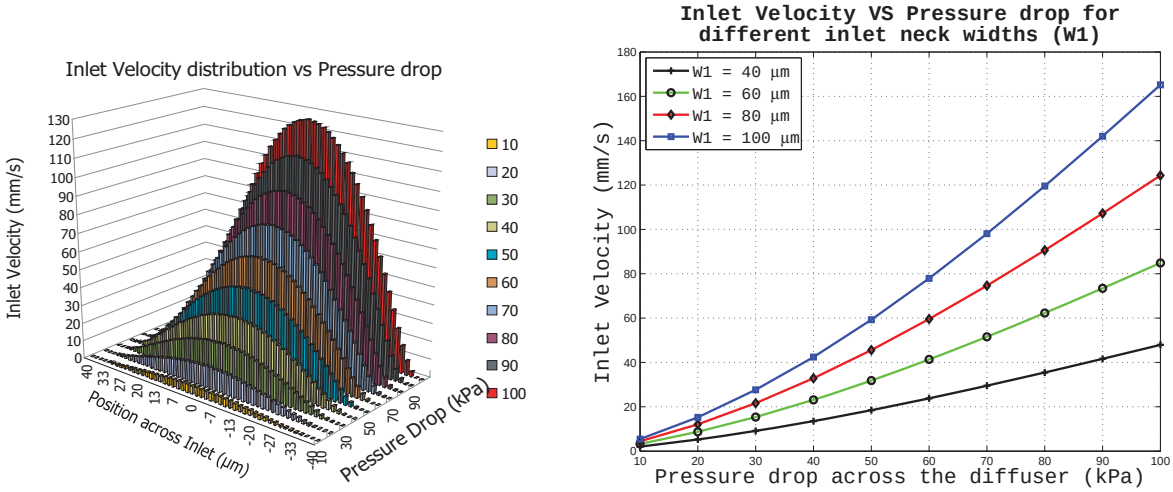

(a) (b)

Figure 5.10. Diffuser performance analysis. (a) Inlet velocity variation for different pressure drops across the inlet neck width $W1$. (b) Inlet velocity variation for different pressure drops across the diffuser for different diffuser neck widths.

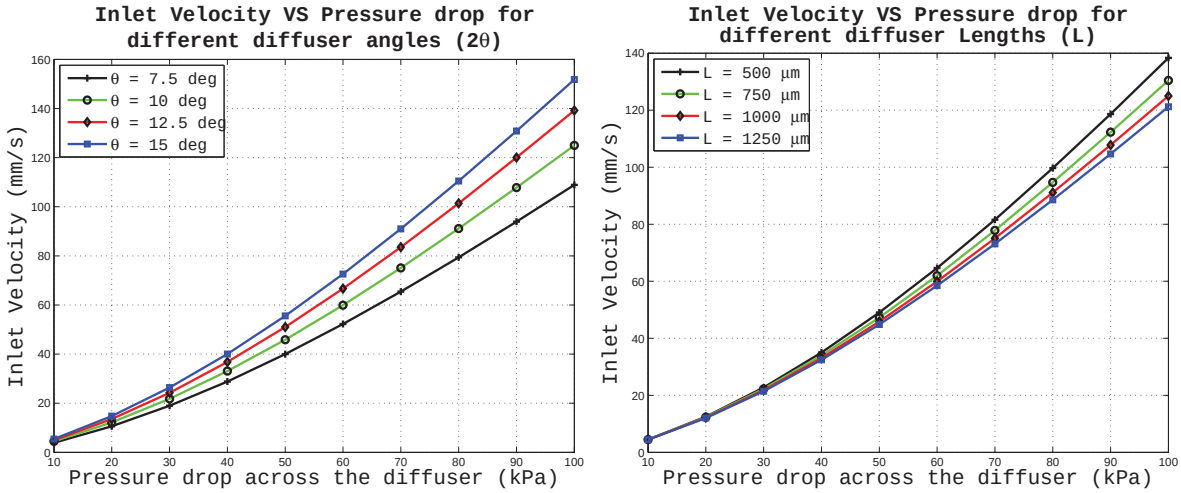

(a) (b)

Figure 5.11. Flow velocity against diffuser parameters 2θ and L. (a) Inlet velocity variation for different pressure drops across the diffuser for different diffuser angles. (b) Inlet velocity variation for different pressure drops across the diffuser for different diffuser lengths.

As the diffuser length is increased, the inlet velocity is also decreased for respective pressure drops. Therefore for higher flow rates, shorter diffusers are desired.

Previously, Olsson *et al.* (1996) have designed and analysed 2D diffuser elements using basic FEA, that was subjected to limitations such as less node density in the finite element model, as well as low processing power. However, they were able to validate their modelling using experimental results. Therefore, their work was considered as a benchmark for the 2D analysis of diffuser elements in this thesis. In this research however, 2D analyses of diffuser elements were first carried out using FEA with more design capability and high processing power, compared to the work reported by Olsson *et al.* (1996).

As a result, it was noted that the flow patterns and pressure distributions observed in Figure 5.8 are closely related to the results presented by Olsson *et al.* (1996). Furthermore, the dependency of the inlet velocity (hence the flow rate) on diffuser parameters were understood. Therefore, based on these FEA results the optimal diffuser parameters can be selected to facilitate optimal operational conditions for flow rectification. However, the effect of the Reynolds number on the fluid flow is also need to be considered, to have a laminar flow instead of a turbulent flow, which would strongly depend on the specific application.

5.3.3 3D–CFD Simulations of Flat–walled Diffusers

Researchers have previously published numerical simulations based analysis of diffuser elements. However, these are mainly based on 2D models. In some cases, simplified 3D models have been analysed due to the limitations set by simulation tools, and limited processing power (Olsson 1998). Additionally, some of the analysis on pressure loss has been carried out for very low Reynolds numbers (< 50) or very high Reynolds numbers ($> 10^5$) (Jiang *et al.* 1998), where results are not directly comparable with flows with intermediary Reynolds numbers.

Furthermore, researchers have worked on analysing diffusers with different diffuser angles, and for sharp and well–rounded inlets to the nozzle–diffuser elements, and with sharp outlets (Olsson *et al.* 1996, Gerlach 1998, Singhal *et al.* 2004), however, these results are not accurate for flow scenarios with low to medium range Reynolds numbers in different diffuser dimensions.

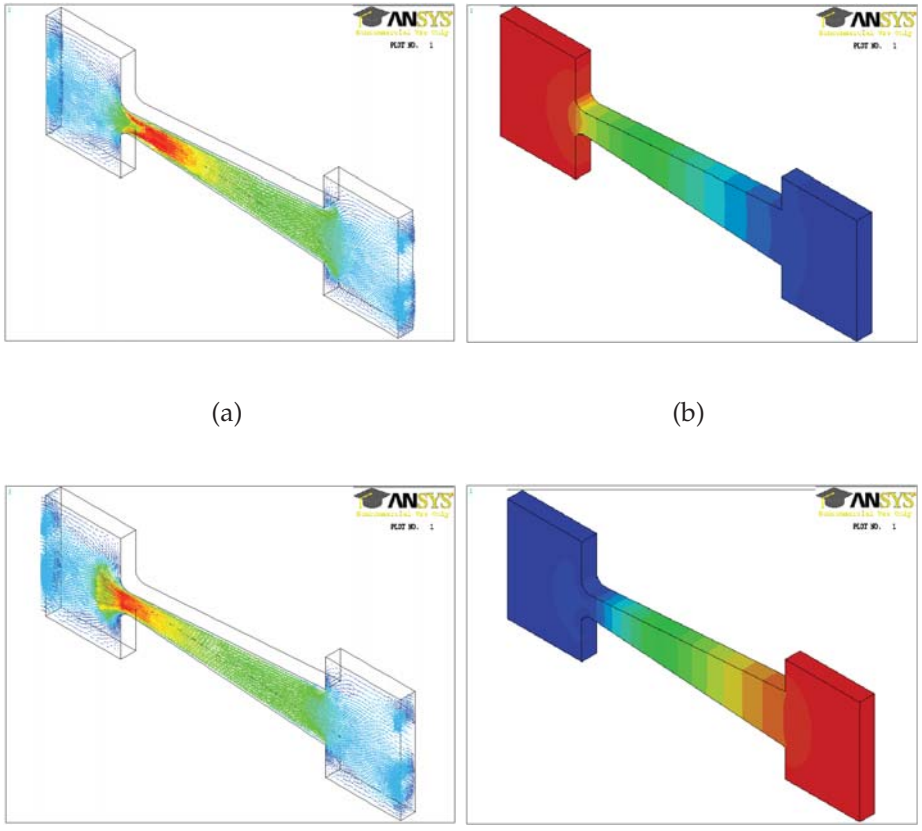

(a) (b)

(c) (d)

Figure 5.12. 3D diffuser simulation results. (a) Vector plot of the velocity in diffuser direction, (b) Pressure distribution of the diffuser in diffuser direction. (c) Vector plot of the velocity in nozzle direction, and (d) Pressure distribution of the diffuser in nozzle direction. The velocity across the neck is much higher than that of any other cross–section of the diffuser element. The laminar flow is realised throughout the diffuser without flow separation for low Reynolds numbers (< 1000).

Based on this review of the literature, it is clear that a separate independent analysis of diffuser elements is best suited, instead of relying on simulations and analysis that were based on different regions in spectrums of diffuser parameters, and incompatible range of flow conditions. Some of the researchers in the field has also recognised the presence of conflicting results specific to diffuser analysis (Singhal *et al.* 2004), which also highlights the importance of carrying out independent analysis. Additionally, with the availability of advance versions of simulation tools, and high speed and powerful processors, more rigorous and complex 3D analysis can be carried out. In this section therefore, the need for developing a clear understanding of the flow behaviour

through diffuser elements at low Reynolds numbers is addressed and results obtained through 3D modelling of the diffusers are presented.

The simulations were carried out using the FEM, and ANSYS was used to model and solve the flows. Both transient and steady state analysis were carried out and performance was analysed for various diffuser parameters. Figure 5.12 shows the velocity and pressure distribution of 3D diffuser elements in both diffuser and nozzle directions. It can be noted that, similar to the 2D analysis, higher velocities are observed near the neck of the diffuser.

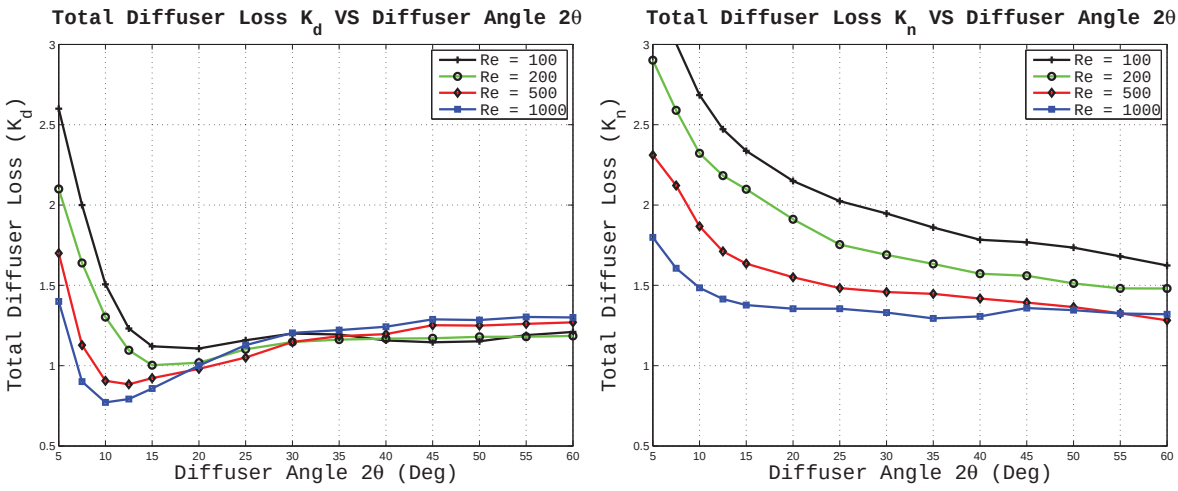

(a) (b)

Figure 5.13. Total pressure loss in a diffuser. Plot of variation of total pressure loss coefficient in a flat–walled diffuser with diffuser angle 2θ, for Re = 100, 200, 500 and 1000. (a) In diffuser direction and (b) In nozzle direction.

Figure 5.13 presents the numerical total pressure loss coefficients of the microdiffusers. The simulations are carried out for Reynolds numbers ranging from 100 to 1000. In general, these simulation results are in a good agreement with the published research (Singhal *et al.* 2004, Wang *et al.* 2008) for low Reynolds number analysis. However, for medium diffuser angles, the predictions in this research show higher values of diffuser loss.

In Figure 5.14 (a), the variations of numerical total losses with Reynolds number for diffusers with diffuser angles 2θ = 5, 10, 30, and 40 are presented. Clearly, diffusers with smaller diverging angles show a strong dependence of K_d on Reynolds number;

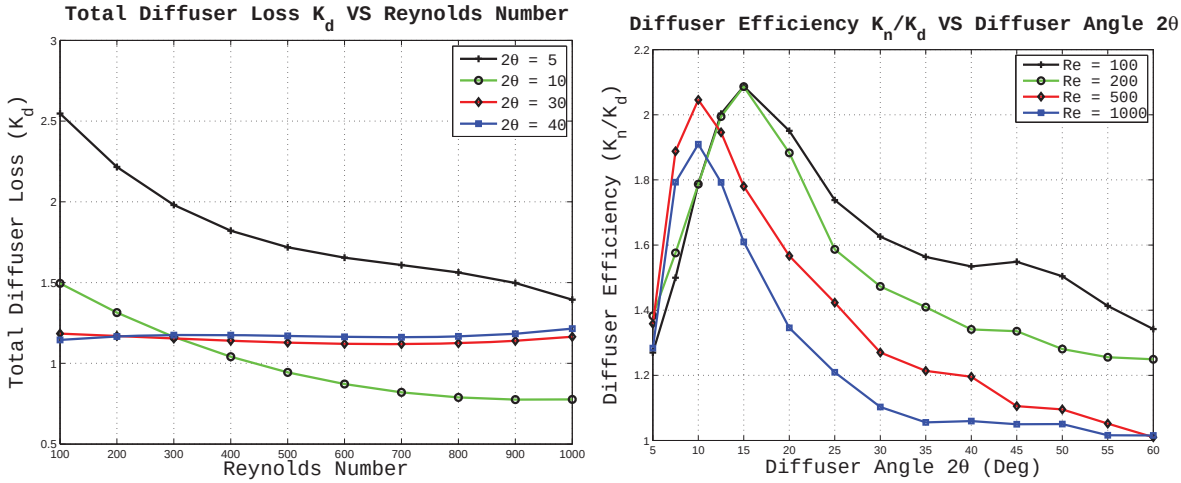

(a) (b)

Figure 5.14. Diffuser Efficiency. (a) Plot of variation of total pressure loss coefficient in a flat–walled diffuser with Re for $2\theta = 5$, 10, 30 and 40. (b) Plot of variation of total diffuser efficiency in a flat–walled diffuser with diffuser angle 2θ, for Re = 100, 200, 500 and 1000.

the loss coefficient decreases monotonically with increasing Reynolds numbers. The loss coefficient for the small–angled diffusers at low Reynolds numbers is greater than those for large–angled diffusers. Furthermore, for small diverging angles the diffuser flow is found to be "separation–free". For increased diverging angles, the flow separation occurs at some critical Reynolds number and K_d becomes insensitive to Reynolds number. Furthermore, at comparatively higher angles, the influence of Reynolds number on the variations in K_d is small, compared to other regions.

Figure 5.14 (b), depicts the overall diffuser efficiency for the designed 3D model. Based on these simulations, diffusers with relatively small angles have a better flow rectification property than ones with large angles. For all Reynolds numbers, the diffuser efficiency η, first increases with increasing diffuser angle, reaches an optimum value, and then decreases substantially. The optimum diffuser angle is located at 15° for Re = 100 and reduces to 10° for Re = 1000.

5.4 Chapter Summary

Diffuser elements were chosen as the flow directing valves for the proposed micropump structure, and were analysed in this Chapter. Computational Fluid Dynamics (CFD) based flow characteristics of diffuser elements were analysed and presented. Microfluidic flow characteristics of low Reynolds number laminar flow through gradually expanding flat–walled diffusers were investigated. A detailed theoretical analysis of diffuser elements, and the relationship between the dimensions and the performance were presented and discussed. ANSYS based FEM and FEA results are discussed to highlight the importance in parameter optimisation.

The results from the numerical analysis were quantified in terms of pressure loss coefficient. The pressure loss coefficients were used to calculate the diffuser efficiency for 3D diffuser elements. Contrary to past claims, flow rectification is shown to be possible for laminar flows. Based on the analysis carried out in this chapter, a diffuser with effective flow rectification capabilities is implemented in the modelling of micropumps and detailed results are presented in Chapter 6.

Chapter 6

3D Multi–Field Analysis of the Micropump

THIS chapter presents multi–field analysis of a novel Surface Acoustic (SAW) device based, electrostatically actuated, valveless micropump, which is designed for *in–vivo* applications such as nanoliter drug delivery. Finite Element Analysis (FEA) based multi–field analysis is developed and carried out to perform detailed Computational Fluid Dynamics (CFD) analysis of the device.

The Fluid–Solid Interactions (FSIs) of the device is effectively modelled using a multiple code coupling capacities in ANSYS and CFX tools. Both preliminary and detailed 3D modelling results are presented, and the pumping action is clearly demonstrated.

Moreover, the effect of convergence settings on accurate simulation results is presented, and the damping effects that is introduced by the fluid domain on the microdiaphragm performance is investigated. A successful estimation of the micropump flow rate is also presented, and the potential future implementations of such complex modelling technology in microfluidic device analysis is also addressed.

6.1 Introduction

Micro electro mechanical systems (MEMS) technology is increasingly being applied to develop drug delivery and related microfluidic devices to facilitate various dosing methods. MEMS based drug delivery devices in general include microneedles, osmosis devices, micropumps and biodegradable MEMS devices (Nisar *et al.* 2008b). Moreover, over the past two decades, significant progress has been made in the development of microfluidic devices based MEMS technologies, such as micrototal analysis systems (μTAS), biochemical microsensors, microvalves, and micropumps (Chen *et al.* 2008). Importantly, microfluidic technologies incorporate the interaction of MEMS devices and surrounding fluids.

There are many instances where successful realisation of micropumps have lead to a range of useful applications. Implantation of completely microfabricated pump has been reported, and has demonstrated the potential capability in implantation of micropumps at various anatomical positions (Maillefer 2003, Leung *et al.* 1998). Various other implantable drug delivery systems that are based on subsystems such as micromachined parts or sensors for pump control, remotely activated capsules, and micro–pills with drug reservoirs are presented in literature (Deo *et al.* 2003, Prescott *et al.* 2006).

Based on the working principle of micropumps, they can be classified under a host of categories such as electromagnetic, electrostatic, piezoelectric, shape memory, bimetallic, etc (Nguyen *et al.* 2002, Nga *et al.* 2004). Electrostatic micropumps have attracted attention in recent years since electrostatic actuators can easily be miniaturised and the electrostatic force between two capacitor plates depends only on a few parameters such as the applied voltage, the dielectric media, the distance between the plates, and the effective plate area (Nga *et al.* 2004).

Numerical modelling of electromechanical fluid coupling in micropumps has also been investigated by many researchers (Cui *et al.* 2008, Lee and Kim 2006). However, most of these modelling have been on piezoelectric micropumps and the coupled field analysis has been conducted on simplified 2D models of the micropump. Nisar *et al.* (2008b) presented an analysis of a piezoelectric micropump using multiple code coupling (MFX) capabilities in ANSYS, which requires only one interface between the physics fields (Fluid–Solid). However, in electrostatically actuated micropump analysis, the design is more advanced as there are two interfaces involved between Fluid–Solid and Solid–Air fields.

Even the design process of the piezoelectrically actuated valueless membrane micropump is considered to be very complex, as it requires expert knowledge of electronics, material properties, solid mechanics and microfluidics (Nisar *et al.* 2008d). Based on published research, numerical study of the valveless micropumps are mostly based on lumped mass model (Olsson *et al.* 1996), simplified dynamic systems model (Gerlach 1998), and various analytical models (Hsu and Le 2008, Squires and Quake 2005), including equivalent circuit models (Hsu and Le 2008). However, as a developing trend FEM and CFD based analysis of microfluidic devices have been carried out by various researchers (Nisar *et al.* 2008d, Tsui and Lu 2008, Yao *et al.* 2007).

In carrying out CFD based transient analysis for micropump modelling, various researchers have utilised low operating frequencies for initial modelling and analysis. For instance, Yao *et al.* (2007) have carried out CFD analysis with frequencies 8 – 500 Hz for their micropump, while Nisar *et al.* (2008d) have used 10 – 200 Hz to analyse their piezoelectrically actuated micropump. However these models have used high actuation voltages up to 140 Volts, to achieve a desired level of performance.

As a result, the demanding importance in developing advanced modelling and analysis capabilities for low–powered micropumps has been identified, especially the importance for a fully passive micropump for drug delivery. Hence, a 3D multi–field analysis of an electrostatically actuated valveless micropump, utilising multiple code coupling capabilities in ANSYS, simultaneously combined with ANSYS–CFX is presented.

The organisation of this chapter is as follows. In Section 6.2, an explanation of the operation of the micropump structure is given, and in Section 6.3 a theoretical model is illustrated using bending theory of plates and Navier–Stokes equations. Then ANSYS and CFX based, modelling and simulation process, and multi–field simulation procedure are explained in Sections 6.4 and 6.5, respectively. 3D multi–field analysis of the electrostatically actuated, valveless micropump is then presented in Section 6.6. Detailed modelling of preliminary and full 3D micropump models, and their CFD analysis based results are described in Sections 6.7 and 6.8, respectively. Finally, the concluding remarks are presented in Section 6.10.

6.2 Micropump Design and Operating Principle

As was illustrated in Chapter 2, the proposed micropump is interrogated using conventional RFID technology where low power circuits can obtain their power from an electromagnetic field. As elaborated in Figure 6.1, micropump structure consist of a thin conductive microdiaphragm, a pumping chamber, and inlet and outlet made of flat–walled diffusers. The gap between the conductive microdiaphragm and the output IDT of the SAW device is set to be a few micrometers for effective low–power actuation of the microdiaphragm. A component level detailed analysis on microdiaphragm, and flat–walled diffuser performance were presented in Chapters 4 and 5, respectively.

In this chapter, the analysis of a full 3D model of the micropump is presented. Furthermore, FEA based CFD modelling and simulation results are presented in order to estimate the micropump performance under a low actuation signal.

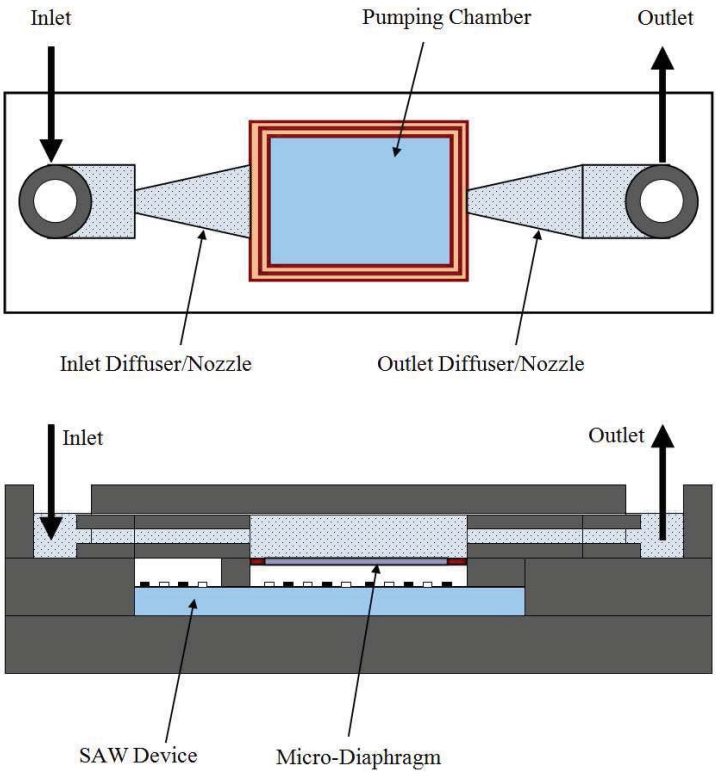

Figure 6.1. Two dimensional views of the micropump. TOP: Top view of the micropump; consists of inlet and outlet diffuser elements for flow rectification, pumping chamber and microdiaphragm. BOTTOM: Side view of the micropump; pumping chamber with the microdiaphragm placed on top of the output IDT of the SAW device.

6.3 Theoretical Analysis of Actuation

In most of the microdiaphragm based micropump mechanisms, the deflection of the microdiaphragm is very small compared to the typical length of the microdiaphragm. Therefore bending theory of plates is applicable and the transverse deflection for the microdiaphragm can be expressed as (Cui *et al.* 2008, Lee and Kim 2000):

$$\mathbb{D}\nabla^4 W_D + \rho_D t_D \frac{\partial^2 W_D}{\partial t^2} = F - P, \tag{6.1}$$

where the bending stiffness $\mathbb{D} = \frac{\mathbb{E}{t_D}^3}{[12(1-\nu^2)]}$, $\mathbb{E}$ is the modulus of elasticity, t_D is the microdiaphragm thickness and ν is the Poisson ratio of the microdiaphragm material. Moreover, W_D is the instantaneous deflection of the pump diaphragm, ρ_D is the density of the microdiaphragm material and ∇^4 is the two dimensional double Laplacian operator. Additionally, F is the actuating electrostatic force acting on the microdiaphragm as shown later in Equation 6.2, while P is the dynamic pressure imposed on the microdiaphragm by the fluid as shown in Equation 6.3. The existence of F and P in this micropump structure is considered in detail in following sections.

6.3.1 Electrostatic Force Generation

As was previously discussed in Chapters 3 and 4, in electrostatic actuation, the electrostatic force applied on electrostatic plates can be described using the parallel plate capacitor effect,

$$F = \frac{1}{2}\frac{\varepsilon A \Phi^2}{(h - W_D)^2}, \tag{6.2}$$

where ε is the dielectric coefficient of the medium between the plates, A is the effective plate area, W_D is the instantaneous deflection of the microdiaphragm, h is the initial plate spacing, and Φ is the applied electric potential between the plates.

However, as was described in Chapter 3, in SAW device based electrostatic actuation, electrostatic force is generated due to the time varying electric potential at the output IDT and the conductive microdiaphragm. This results in a more complex force than the force shown in Equation 6.2.

6.3.2 Microfluidic Pressure Variation

The mass transport in microfluidic devices is generally dominated by viscous dissipation, while inertial effects are generally considered to be negligible (Squires and Quake 2005). In electrostatically actuated micropumps, the fluid flow is considered to be incompressible. Furthermore, non-slip boundary conditions (non-turbulent flow) are assumed to exist at micropump walls. The governing equations for viscus, incompressible fluid flow can be written using Navier–Stokes equations and mass continuity equation as

$$\rho_L \frac{dV}{dt} = \rho_L g + \mu \nabla^2 V - \nabla P, \tag{6.3}$$

$$\frac{\partial \rho_L}{\partial t} + (\nabla \cdot V)\rho_L = 0, \tag{6.4}$$

where V is the fluid velocity vector. μ is the viscosity, g is the gravitational acceleration, ρ_L is the density, and P is the dynamic pressure of the fluid.

These governing equations show that the electrostatic actuation force, the deflection of the microdiaphragm and the flow of the working fluid are always coupled during the pumping action, in an electrostatically actuated valveless micropump. In order to analytically determine the deflection of the microdiaphragm due to excitation force, Equations 6.1– 6.4 are required to be solved simultaneously.

In general, the analytical modelling of full 3D fluid flow requires complex algorithms and extensive computational effort. However, various researcher have successfully analysed such scenarios through numerical analysis and mathematical methods such as FEA (Nisar *et al.* 2008b, Bao 2000).

As a novel contribution to the microfluidic device analysis, multiple code coupling based simulation methodology is deployed to analyse the complex coupling between multiple physics fields. Therefore the electrostatic, structural and fluid field couplings is simulated and the Fluid–Solid Interaction (FSI) analysis of the micropump is developed and presented.

6.4 Modelling and Simulation of Micropump

Based on the published research (Yao *et al.* 2007, Nisar *et al.* 2008d, Nga *et al.* 2004), till now there are very few accurate and broadly applicable models developed for 3D

micropump design and analysis. Even in such analysis, researchers have analysed simplified models, with some associated assumptions. During this research, a simplified 3D model was first developed to build the confidence in FEA based CFD analysis and then carried out a full 3D analysis of the device, without any compromise in model features.

The CFD analysis was carried out in two stages; initial design stage and the final performance analysis stage. During the initial design stage, firstly the aforementioned simplified 3D model was developed and analysed, which is well discussed in Section 6.7. Once the initial design was simulated and analysed, then a full 3D model was developed and CFD analysis was carried out, as presented in Section 6.8. During this analysis, the performance of the micropump was investigated for various material properties, control parameters, and environment parameters. Then for a specified set of such parameters, as depicted in Figure 6.2, repetitive analysis was carried out only by varying design parameters until the performance was optimised. Once the design was optimised for its performance, then various analysis were carried out to specify final performance characteristics of the micropump.

In carrying out ANSYS and CFX based analysis, it is important to set accurate convergence criteria and relaxation factors in Fluid–Solid Interaction (FSI) analysis of microdevices (Nisar *et al.* 2008d, ANSYS Incorporation 2009b). Therefore care was taken during the initial iterative analysis to fine tune such parameters for smoother simulations. The ANSYS based multi–field solution process is of great importance in performing FSI analysis of the micropump.

6.5 Multi–Field Solution Process

The Multi–field solver with multiple code couple capability (MFX) in ANSYS was chosen to simulate and investigate the 3D Fluid–Solid Interaction (FSI) scenario for the micropump. The MFX solver is one of two versions of the ANSYS Multi–field solver. The other version ANSYS–MFS, was previously utilised for the analysis of microactuator and microdiaphragm performance in Chapters 3 and 4. Here, the MFX solver is best suited for 3D FSI analysis, due to its capability to carry out more physically complex and larger simulations with distributed physics fields.

The solution process applicable for MFX is shown in Figure 6.3. Here, the ANSYS code acts as the master and reads all MFX commands, does the mapping, and serves the time

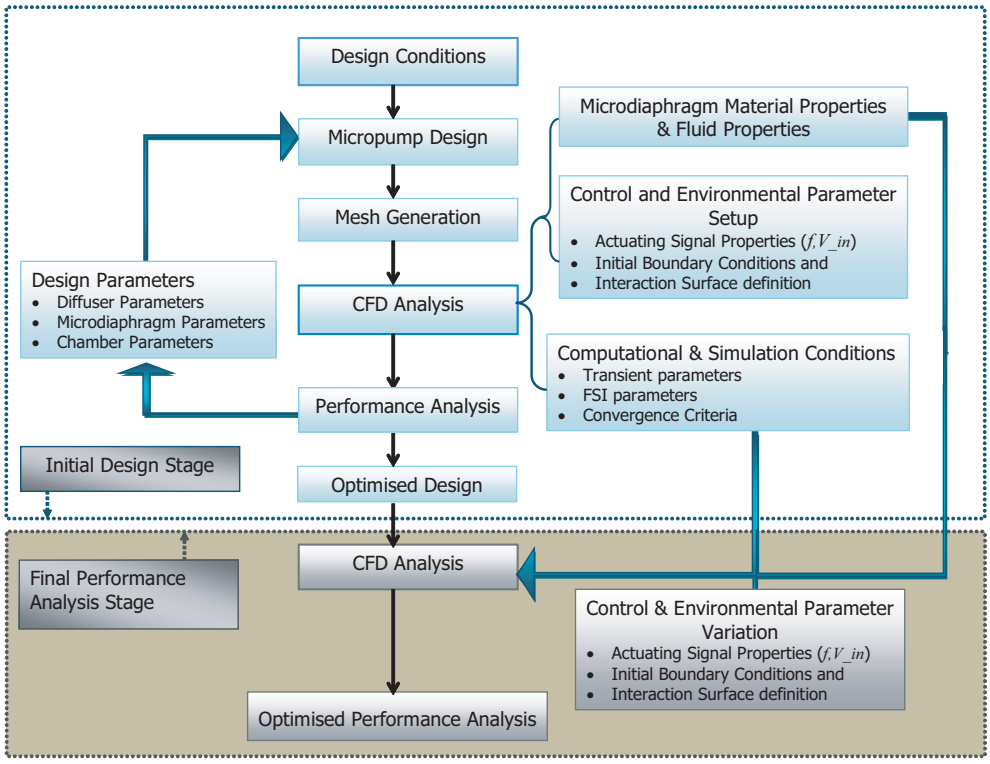

Figure 6.2. Design and performance analysis stages of FEA based CFD analysis of the 3D micropump structure. The CFD analyses consist of two stages; initial design stage and the final performance analysis stage. At the initial design stage, the performance of the micropump is investigated for various material properties, control parameters, and environment parameters. For a specified set of such parameters, a repetitive analysis is carried out by varying design parameters until the performance is optimised. Once the design is optimised for its performance, various analyses were carried out to specify final performance characteristics of the micropump.

step and stagger loop controls to the CFX, which act as the slave. The solution process consists of two loops; the multi–field time loop and the multi–field stagger loop. As depicted in Figure 6.3, a stagger loop runs within each time step. The stagger loop allows for implicit coupling of the fields in the MFX solution. Within each step in the time step loop, the field solutions are repeated in the stagger loop until convergence. It should be noted that the number of iterations executed within the stagger loop is determined by the convergence of the loads transfer between fields, or the maximum number of stagger iterations, which is set during the initial problem setup. Once the load transfer is completed, the global convergence is checked. If global convergence of the load transfer is not achieved, another stagger loop is performed. Otherwise, the

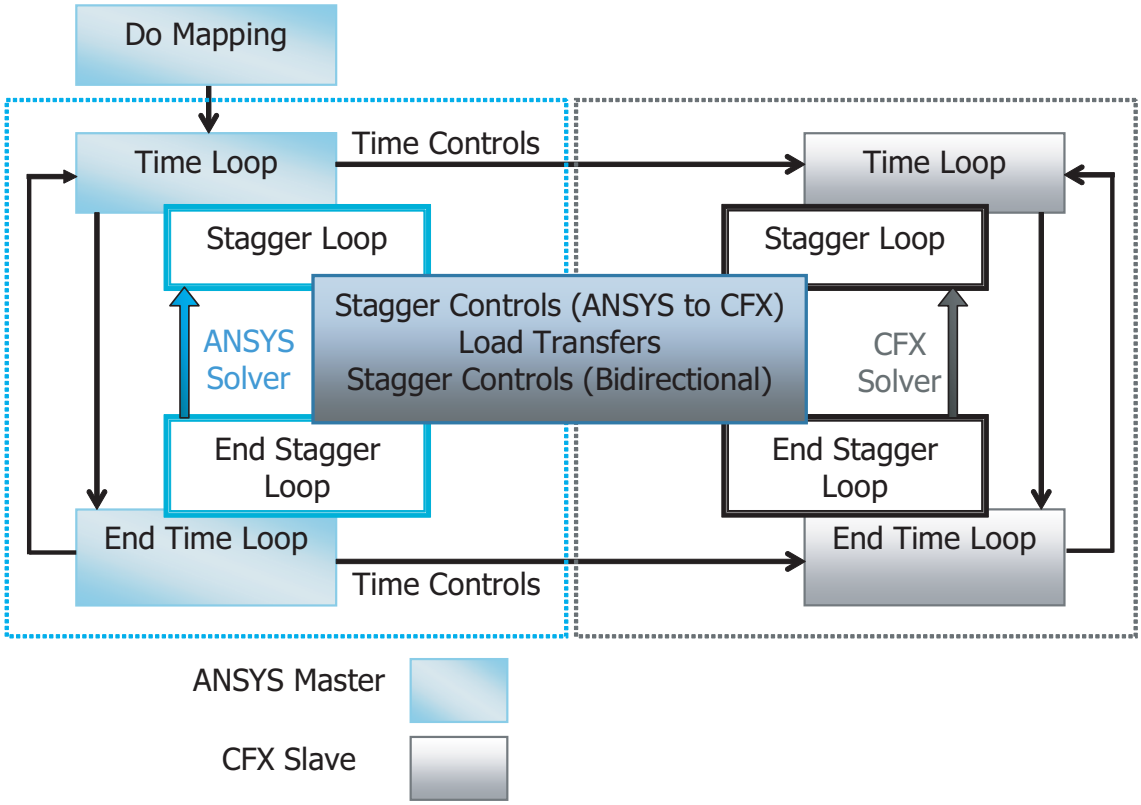

Figure 6.3. ANSYS and CFX code interaction during MFX based multiple code coupling simulations. During FSI analysis of the micropump, ANSYS code acts as the master while CFX code acts as the slave. Within each ANSYS time loop, several stagger iterations are executed while communicating with CFX code.

simulation moves on to the next time step and follow the same procedure as explained above. This procedure is repeated until the code is executed for the full time interval of the simulation.

6.6 3D CFD Analysis of Micropump

Based on the published research, most of the FSI analysis has been carried out on piezoelectrically actuated micropumps (Nisar *et al.* 2008b, Nisar *et al.* 2008d, Yao *et al.* 2007, Cui *et al.* 2008), where only two physics fields are interacting (piezoelectric and fluid). Only limited reports are available on FSI analysis of electrostatically actuated micropumps (Teymoori and Abbaspour-Sani 2004, Bourouina *et al.* 1997). Moreover, these

analyses have adopted simplified models, instead of carrying out full 3D CFD analysis, and have not taken into account the coupled multi–field effects of microdiaphragm deformation and fluid structure interface.

More importantly, for a full dynamic analysis of electrostatically actuated micropumps, three physics fields are needed to be analysed simultaneously (coupling between air field, solid structure, and fluid region), which results in a complex problem to solve. Therefore, in this research, the importance in advanced modelling and analysis of an electrostatically actuated micropumps is addressed, and a full 3D model is developed for performance analysis.

In order to dictate dynamic performance characteristics of such a microfluidic device, first a simplified 3D model was developed in ANSYS. Here, the actuation mechanism is based on electrostatic forces generated between the SAW device and the microdiaphragm. Moreover, the electrostatic force is dependant on the instantaneous microdiaphragm displacement as was discussed in Chapters 3 and 4. Therefore, in addition to the coupling between the microdiaphragm and the microfluidic region, the transient coupling effect between the air–gap and the microdiaphragm is required to be incorporated into the analysis.

In solving this problem, a multiple solvers in ANSYS and CFX were utilised. A direct coupling analysis was carried out in ANSYS master code to analyse the electrostatic coupling effects, while using ANSYS CFX solver to analyse the microfluidic flow in the fluid domain. Importantly, the ANSYS multi–field solver with multiple code coupling features (MFX) was utilised to analyse the whole structure in a single simulation, by transferring necessary interface boundary conditions between ANSYS and CFX field solvers.

Once the confidence was developed after carrying out initial FSI analysis, a full 3D model was developed and investigated including all the necessary components of the SAW device based micropump structure.

6.7 Preliminary 3D Model Development

The preliminary micropump model is designed as shown Figure 6.4. Necessary electrical and mechanical boundary conditions are applied on the design to mimic the expected physical constrains. During initial modelling, a thin 3D section of the valveless micropump is designed for simplicity. Furthermore, to analyse the diffuser and

nozzle effects of inlet and outlet of the micropump, a single opening is included. The advantage in this method during initial modelling is that the simulation time can substantially be reduced by exploiting the half–symmetry of the micropump.

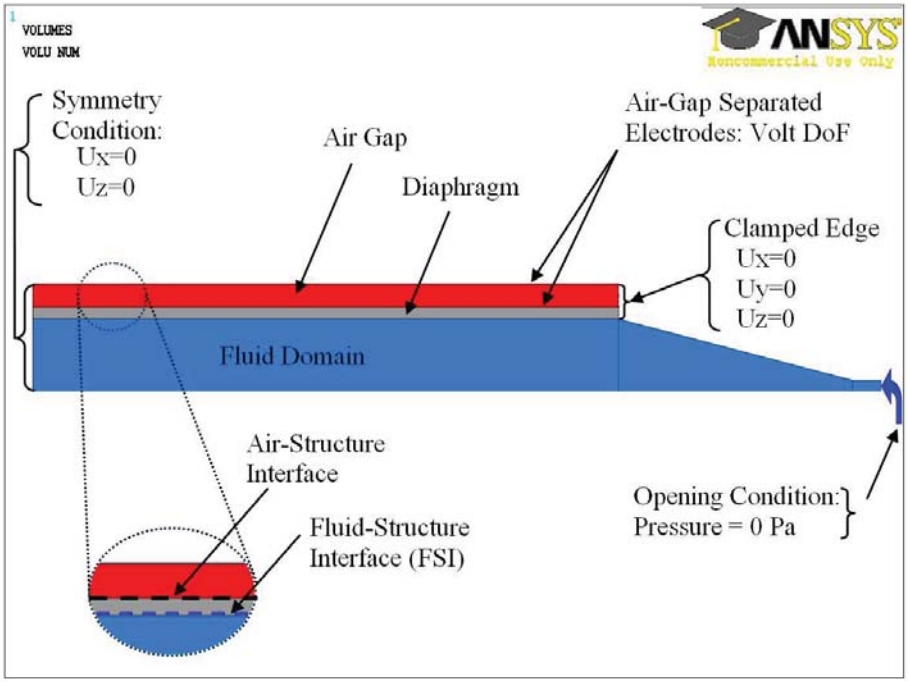

Figure 6.4. A side view of the simplified initial 3D model. Two interface boundaries are identified in the micropump model. Air–Structure Interface (ASI): between the microdiaphragm and the air–gap. Fluid-Structure Interface (FSI): between the microdiaphragm and the fluidic chamber. Symmetry is exploited to reduce the simulation time and CPU usage. For ease in visualisation, the microdiaphragm is placed on top of the pumping chamber during the analysis. Dimensions: Chamber length = 1250 μm, Chamber height = 150 μm, Diffuser length = 550 μm, Microdiaphragm length = 1250 μm, microdiaphragm thickness = 20 μm and Air–gap = 20 μm.

As mentioned earlier, two interface boundaries are identified in the micropump model. They are; Air–Structure Interface (ASI), which is between the microdiaphragm and the air–gap, and the Fluid–Structure Interface (FSI), which is between the microdiaphragm and the fluidic chamber. It should be noted that during initial modelling, for ease of visualisation with the simplified design, the microdiaphragm is placed on top of the pumping chamber. The chamber is designed to be 1250 μm in length and 150 μm in height. The diffuser/nozzle length is 550 μm. The microdiaphragm length is 1250 μm and the thickness is set to be 20 μm for initial analysis. The electrodes for electrostatic actuation are separated by a 20 μm air–gap.

Table 6.1. Fluid and material properties used in 3D analysis. Polyimide PI–2610, water and air properties used in 3D simulations (HD MicroSystems 2008, Gad–el–Hak 2002, MEMS and Nanotechnology Clearinghouse 2009).

FLUID AND MATERIAL PROPERTIES FOR 3D FSI ANALYSIS

Material	Property	Value
Polyimide PI-2610	Density (Kg/m^3)	1400
	Poisson's Ratio	0.22
	Elastic Modulus (GPa)	7.5
Water	Density (Kg/m^3)	998
	Viscosity (Ns/m^2)	1.04 e–3
Air	Density (Kg/m^3)	1.205
	Electric permittivity ($pF/\mu m$)	8.854 e–6

During the modelling, the electrostatic analysis problem was designed in ANSYS side. As shown in Figure 6.5 (a), this portion consists of the microdiaphragm, air–gap, and electrodes as coupled nodes (as discussed in Chapters 3 and 4). Top and bottom surfaces of the microdiaphragm are defined by the ASI and FSI, respectively. SOLID95 element type was used for the microdiaphragm model, and SOLID226 was used to model the air–gap. The fluid region was modeled in CFX as depicted in Figure 6.5 (b), and the top surface of the region defines the FSI. Fluid142 element type was used to model the fluid domain, as it is specifically used for the calculation of 2D and 3D velocity and pressure distributions in a single phase, Newtonian fluid (ANSYS Incorporation 2009a). During the CFD analysis, Polyimide PI–2610 was used as the microdiaphragm material and properties of water were used to simulate the fluid flow. The material and fluid properties are presented in Table 6.1.

6.7.1 Simulation Results of the Preliminary 3D Model

Multi–filed simulations based results for the initial model are presented in this section. A transient analysis was carried out in both ANSYS and CFX solvers and the results are presented in this section. In this preliminary analysis, a Direct Current (DC) signal with an amplitude of 10 Volt was applied across the electrodes in the solid model to investigate both the transient and steady state performance of the micropump.

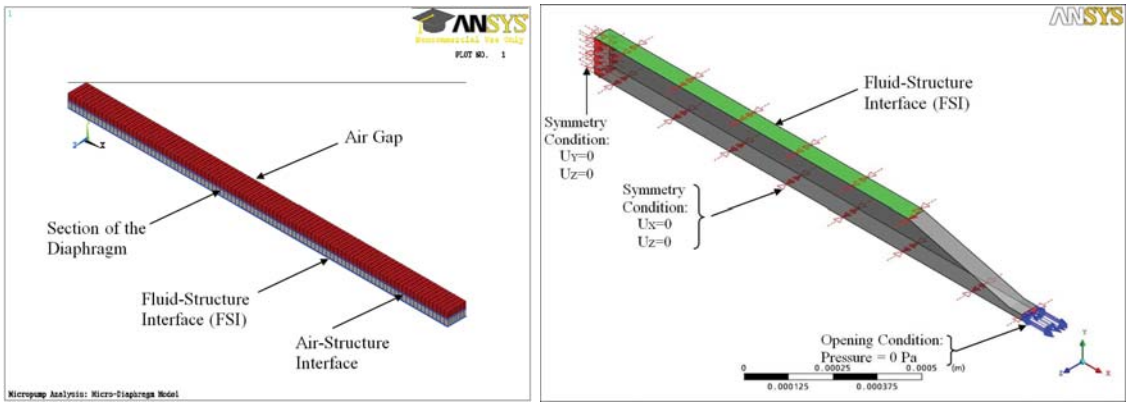

(a) Structural domain (b) Fluid domain

Figure 6.5. ANSYS and CFX models for initial 3D analysis of the micropump consisting of microdiaphragm, air–gap, pumping chamber and diffuser/nozle opening. (a) ANSYS model: Direct coupled–field analysis is used in ANSYS model to simulate the effect of air–gap coupled microdiaphragm. (b) CFX model: A converging opening is designed to investigate the effect of the diffuser/nozzle effect in the CFX model. By implementing symmetric conditions, a thin section of the micropump is modeled in the initial 3D analysis.

As the multi–fluid problem is nonlinear in nature, the convergence is not guaranteed without a careful selection of multi–field solution control parameters such as various convergence and relaxation parameters, multi–field time controls, and coupling frequency between the fields. In such analysis, instabilities could result from a number of factors; the solution matrices may have poor condition numbers because of the finite element mesh or very large gradients in the actual solution. Moreover, the fluid phenomena being observed could be unstable in nature. Therefore, special care was taken to achieve convergence of results during the flow analysis.

At the initial phase of the analysis, multi–field solver parameters were carefully set to achieve a smooth convergence of results. In FEM, factors such as selection of incorrect element types, coarse mesh density, and force convergence criteria, are known to affect the stability of FEA results (ANSYS Incorporation 2009a). During the initial modelling of the micropump, element types were selected carefully to match with the solid and fluid fields, and the model was finely meshed using small element sizes. Therefore, the remaining constraint, the convergence criteria was left for investigation. Especially, the force convergence criteria in the solid model (relate to the direct coupled

solver parameters), was found to be a critical parameter that has a direct influence on smooth and stable results. Various values for force convergence criteria were considered during simulations to determine a suitable parameter value. To demonstrate the influence of such parameters, results obtained through various force convergence settings are shown in Figure 6.6. Based on the results, it is evident that careful selection of convergence values have produced stable transient results with minimal fluctuations.

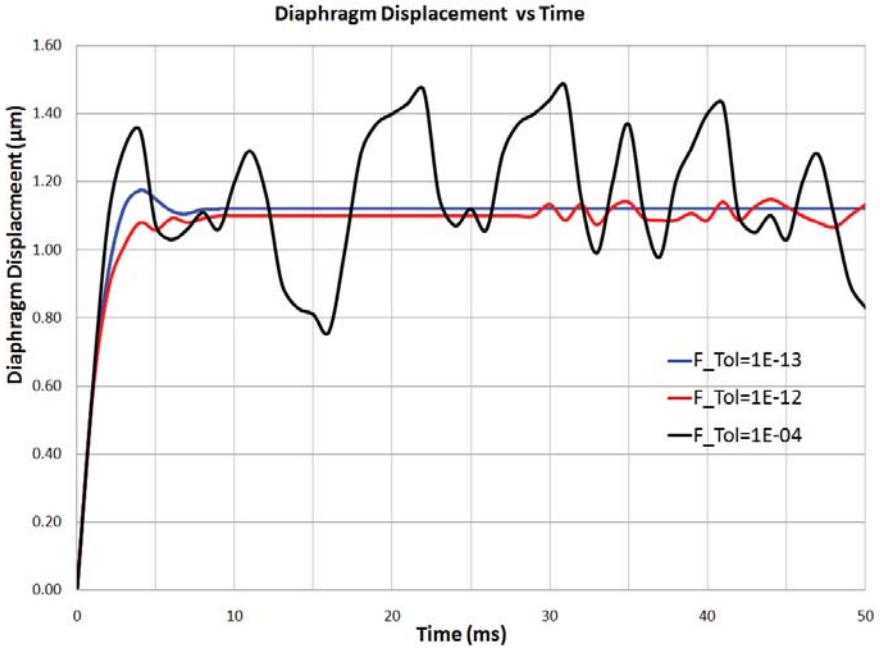

Figure 6.6. Variation in dynamic behaviour of the micropump for various force convergence parameters. Steady results were obtained for *Force Tolerance* value of 10^{-13} and more unstable results were obtained as the tolerance is increased up to 10^{-4}. The flow rate of the micropump can be estimated more accurately for smoother transient results, as it represents a better model.

Following a similar iterative method, CFD results were optimised for the remaining multi–field parameters during the initial 3D analysis. Then the displacement and fluid flow characteristics were investigated. Figure 6.7 depicts a steady state displacement vector plot of the microdiaphragm and combined flow patterns of the fluid domain.

Based on these simulations, higher flow velocities were observed near the entrance of the opening. Additionally, inward velocities at the opening were found to be higher during the supply mode, compared to the velocities during the pumping mode, which demonstrates the diffuser effect of the valveless micropump, hence the pumping action of the device is clearly noted.

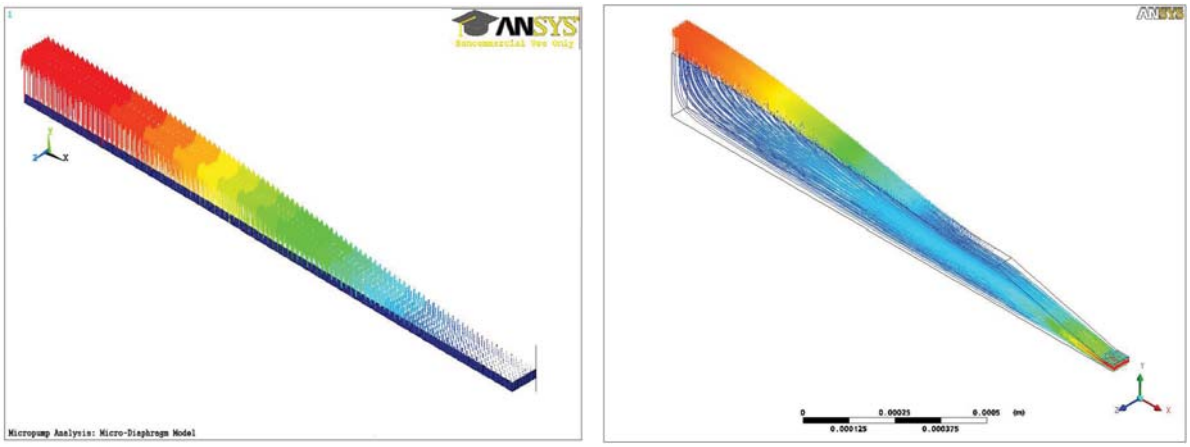

(a) Structural domain (b) Fluid domain

Figure 6.7. Multi–field results of the microdiaphragm displacement and microfluidic flow visualisation in fluid domain. (a) The maximum displacement is achieved at the center of the microdiaphragm. Only a half of the microdiaphragm is modeled for simplicity, by applying symmetric conditions. (b) Combined streamline plot of the fluid flow, and mesh displacement plot at the FSI. Diffuser effect can be observed at the opening. Higher flow velocities are observed near entrance of the opening. Inward velocities at the opening are higher during the supply mode, compared to the velocities during the pumping mode, which demonstrates the diffuser effect of the valveless micropump.

In order to investigate the damping effect caused by the fluid on the microdiaphragm, two different simulations were carried out. One analysis carried out a full simulation considering the Fluid–Solid Interaction (FSI) in the analysis, and another analysis; only considering the electrostatic actuation of the microdiaphragm without the fluid domain. For these simulations, ANSYS based MFX (multiple code coupling capability) and MFS (single code coupling capability) solvers were used respectively. The results are presented in Figure 6.8, and the damping effect caused by the fluid is clearly observed. However, in the general context of micropumps analysis, various techniques have been investigated to minimise the fluid damping effect (Cui *et al.* 2008, Nisar *et al.* 2008b). As such, careful selection of materials and dimensions for microdiaphragms, and operation of the device at frequency away from the resonance frequency of the whole domain, are considered to be effective mechanisms.

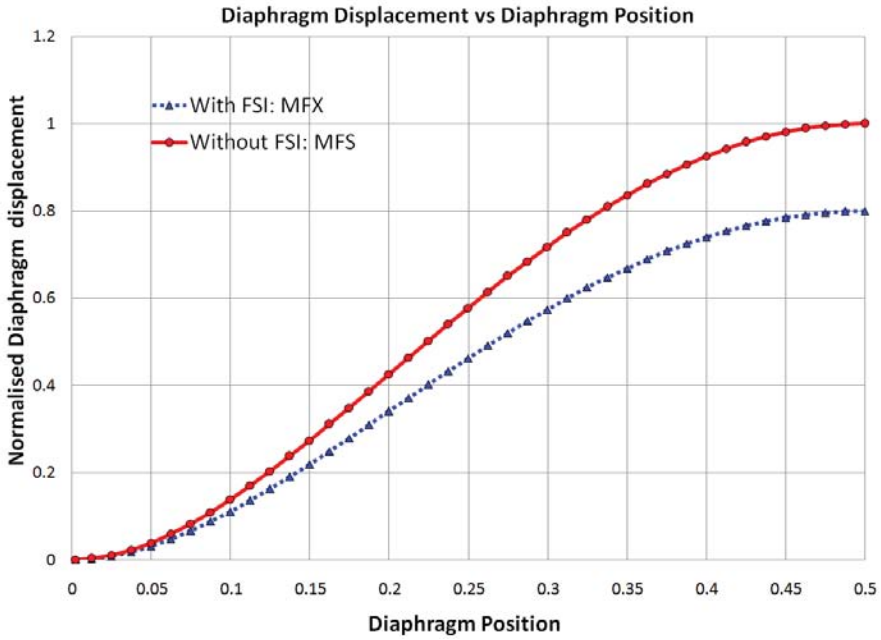

Figure 6.8. Microdiaphragm deformation results. Normalised microdiaphragm deformation along half cross–section of the microdiaphragm, for simulations with and without Fluid–Solid Interaction (FSI). Effects of the fluid damping on the microdiaphragm deflection is clearly noticed.

Therefore, by carrying out different kind of investigations on the developed initial 3D model, the confidence and capability was developed on utilisation of multi–field capabilities for complex Fluid–Solid Interaction (FSI) analysis of micropumps. Consequently, a much more complete 3D design was developed to mimic the behaviour of the SAW based micropump model, consisting of separate inlet and an outlet diffusers. The detailed design of the FEA based CFD investigations are presented in following sections.

6.8 Full 3D Modelling of the Micropump

The full 3D model consists of all the necessary components of the SAW device based valveless micropump as depicted in Figure 6.1. They are inlet, outlet, microdiaphragm, pumping chamber, and the solid model for electrostatic actuation. During this full 3D analysis of the device, half symmetry is exploited without any compromise in model features and accuracy. As a result, the design provides a full representation of the desired micropump. The inlet and the outlet are designed to be flat–walled diffusers

with rounded inlet and sharp outlet, similar to the methodology presented in Chapter 5, and the design of the inlet diffuser is depicted in Figure 6.9.

Since a detailed analysis and discussion of the diffuser elements was presented in Chapter 5, the optimised diffuser parameters were directly utilised to develop diffusers for the 3D micropump model. As such, a diffuser length of 1000 μm, a neck width of 80 μm and a diverging angle of 10° were used. A consistent chamber height of 100 μm was used through out the fluidic chamber. Bidirectional flow conditions are set at both inlet and the outlet, to allow the fluid to flow in and out of diffusers, during supply and pumping modes.

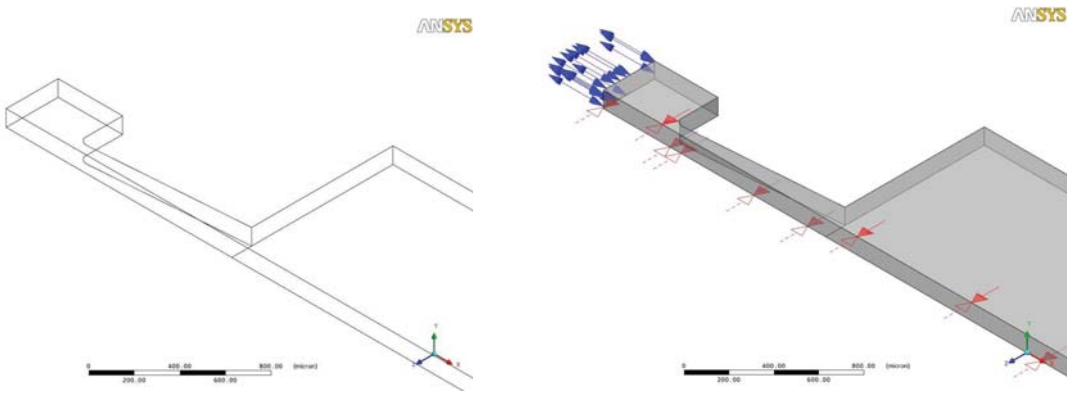

(a) (b)

Figure 6.9. Full 3D model development; microfluidic environment design. (a) The design of 3D flat–walled diffuser elements. The inlet diffuser is connected to the inlet and pumping chamber of the micropump. Diffuser length = 1000 μm, neck width = 80 μm, diverging angle = 10°, and chamber height = 100 μm. (b) Bidirectional flow conditions are set at the inlet and half symmetry is exploited.

The full 3D model of the micropump is depicted in Figure 6.10. As was discussed in Chapter 2, SAW device consists of a piezoelectric substrate, an input IDT and an output IDT. The microfluidic structure is placed on top of the SAW device, such that the microdiaphragm is directly above the output IDT, for electrostatic coupling. Two interface boundaries are identified in the micropump model. They are the Air–Structure Interface (ASI) that is between the microdiaphragm and the air–gap, and the Fluid–Structure Interface (FSI) that is between the microdiaphragm and the fluidic chamber. Half symmetry is exploited to reduce the simulation time and CPU usage, without any compromise in accuracy.

During the multi–field analysis, the interaction at the ASI was completely simulated in ANSYS master code, using direct coupling analysis. Moreover, the interaction at the FSI was simulated in both ANSYS master and CFX slave codes. During this Fluid–Structure Interaction, forces get transferred from fluid region to the solid structure and displacements get transferred from solid structure to the fluid region. The chamber dimensions are 2000 μm $\times$ 2000 μm $\times$ 100 μm (length $\times$ width $\times$ height), and microdiaphragm dimensions are 2000 μm $\times$ 2000 μm $\times$ 5 μm (length $\times$ width $\times$ height). The height of the air–gap beneath the microdiaphragm is set to be 5 μm.

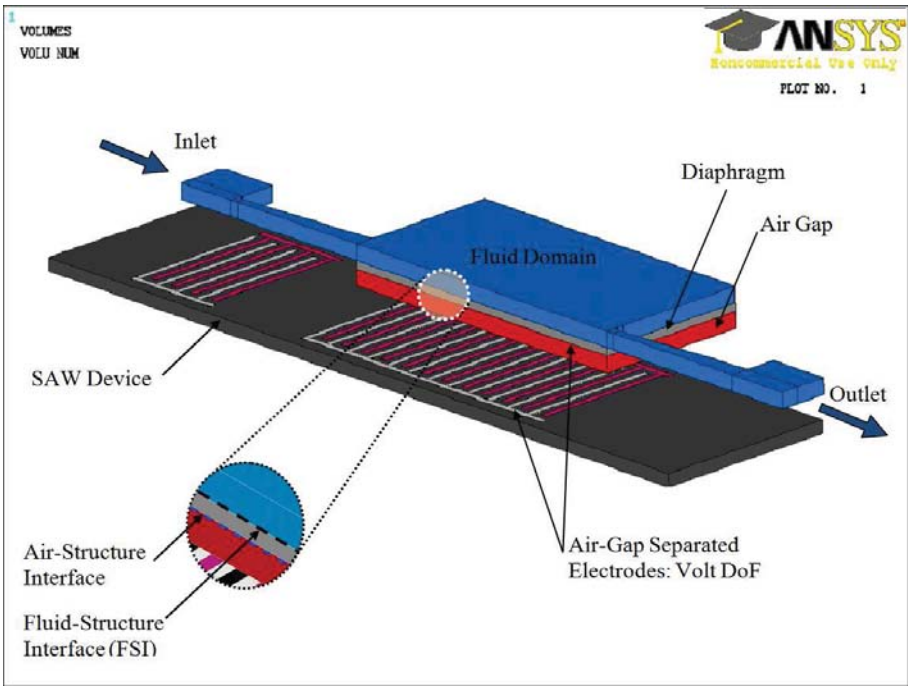

Figure 6.10. Full 3D model development including the SAW device. The microfluidic structure is placed on top of the SAW device for multi–field analysis. Two interface boundaries were identified in the micropump model. Air–Structure Interface (ASI): between the microdiaphragm and the air–gap. Fluid–Structure Interface (FSI): between the microdiaphragm and the fluidic chamber. Half symmetry is exploited to reduce the simulation time and CPU usage, without any compromise in accuracy. Actual gap between the SAW device and the microdiaphragm is set to be a few micrometers. However, for ease in visualisation, a wider gap is left between the microdiaphragm and the SAW device. Dimensions: Chamber length = 2000 μm, Chamber height = 100 μm, Diffuser length = 1000 μm, microdiaphragm length = 2000 μm, microdiaphragm thickness = 5 μm and Air–gap = 5 μm.

It should be noted that in the full 3D model as depicted in Figure 6.10, the micropump structure is mounted on top of the SAW device, hence the pumping chamber is above the microdiaphragm. Whereas in the initial simplified 3D model (Figure 6.4), for simplicity in modelling, the pumping chamber was placed below the microdiaphragm. Importantly, during such Newtonian flow analysis in microfluidic devices inertial forces are small compared to viscous forces (Squires and Quake 2005). Moreover, it is reported that in narrow microfluidic flow channels the gravitational field has negligible effect on the flow characteristics, as the flow behaviour is mainly due to the viscus fluid flow (Jong *et al.* 2007, Yao *et al.* 2004). Therefore, the device orientation has negligible effect on performance, hence there is no measurable adverse effect on the validity of result in this 3D model.

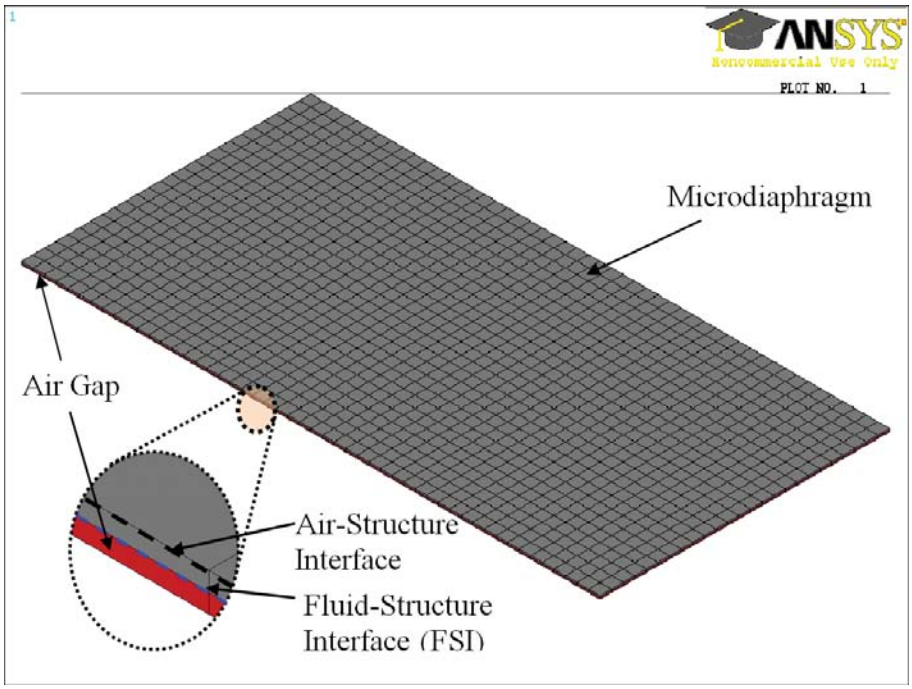

Figure 6.11. ANSYS model for the full 3D analysis of the micropump consisting of the microdiaphragm and the air–gap. Direct coupled field analysis is used to model the solid model consisting of microdiaphragm and the air–gap, to determine the effect of electrostatic forces in electrostatically coupled microdiaphragm. Considering the symmetric conditions, only a half of the micropump is modeled in full 3D analysis. The top and the bottom surfaces of the microdiaphragm interact with the fluid region and the air–gap respectively.

More detailed set up of the solid model is provided in Figure 6.11. The air–gap coupled microdiaphragm is completely modeled in ANSYS master code. During the CFD

analysis, Polyimide PI–2610 is used as the microdiaphragm material. Generally the multi–field solution process consists of large number of solution iterations, hence simulations run for longer periods compared to direct solvers. Therefore to limit this issue, a flat microdiaphragm was designed with less number of nodes, compared to the corrugated microdiaphragm analysis that was presented in Chapter 4. However in doing so, a set of test simulations were performed by varying node density of the model to decide on an optimal node density, such that the variations in results are less than 1 %.

The fluid region setup in CFX is presented in Figure 6.12. A total systems consisting of an inlet diffuser, pumping chamber and an outlet diffuser is developed in CFX. As explained before, flat–walled diffusers are designed to incorporate the valveless effect to the device. Additionally, half symmetry is exploited and the inlet and outlet pressure is set to zero (0 Pa) to investigate the flow rectification effect of flat–walled diffusers, in response to a deflection in the microdiaphragm. Here, water properties were used to simulate the fluid flow. During the analysis, fluid field interacts with the solid structure through FSI, by means of transfer of displacements and forces.

6.8.1 Simulation Results of Full 3D Model

Multi–filed simulations based results for the full 3D model are presented in this section. A full transient analysis is carried out in both ANSYS and CFX solvers. The control signal is mimicked in the solid model by considering an AC sinusoidal with operating frequencies ranging from 1–200 Hz, and 10 Volt peak–peak amplitudes. Therefore, as is presented in Chapter 2, the desired low frequency operation of the device was simulated. It should be noted that the results presented from here on are based on a control signal frequency of 10 Hz. This implies that the interrogated high frequency SAW signal is triggered at a frequency of 10 Hz, so that the effective actuation is in the low frequency range. Simulations were carried out for two time periods consisting of 200 time steps.

Microdiaphragm Displacement Results

Based on the multi–field CFD analysis simulations, the minimum and maximum displacements of the microdiaphragm are depicted in Figure 6.13. Maximum displacements are achieved around the mid section of the microdiaphragm, which is clamped from its sides.

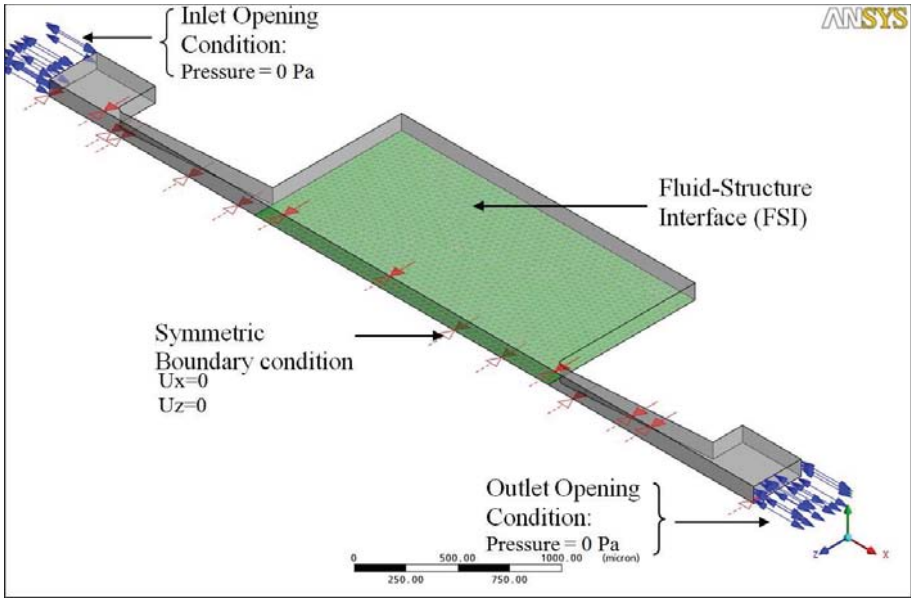

Figure 6.12. CFX model for full 3D analysis of the micropump. For full 3D analysis, a total systems consisting of an inlet diffuser, pumping chamber and an outlet diffuser is developed in CFX. Flat–walled diffusers are designed to incorporate the valveless effect to the device. Half symmetry is exploited, and the inlet and outlet pressure is set to 0 Pa to investigate the flow rectification effect of flat–walled diffusers, in respond to microdiaphragm deflection. During the analysis, fluid field interacts with the solid structure through FSI, by means of transfer of loads.

As can be seen from Figure 6.14, the Fluid–Solid Interface displacement is synchronised with the microdiaphragm displacement. In a 200 steps simulation, step 25 relates to the first peak of the control signal. From steps 1 to 25, a gradual increase in the interface deflection can be noted. Then the deflection gradually reduces back to the reference level by step 50. This periodic pattern is repeated until the simulation ends.

As a result of using a thin microdiaphragm made of flexible but stable material, the mid section of the microdiaphragm has maintained its flatness. As the amplitude of the control signal is increased, the displacement of the microdiaphragm is also increased and a higher chamber volume is created. Hence the pressure inside the chamber is increased compared to the pressure at the inlet and outlet. Then, as the amplitude of the control signal is decreased, the displacement of the microdiaphragm is also decreased and the chamber volume is decreased. As a result, the relative chamber pressure is

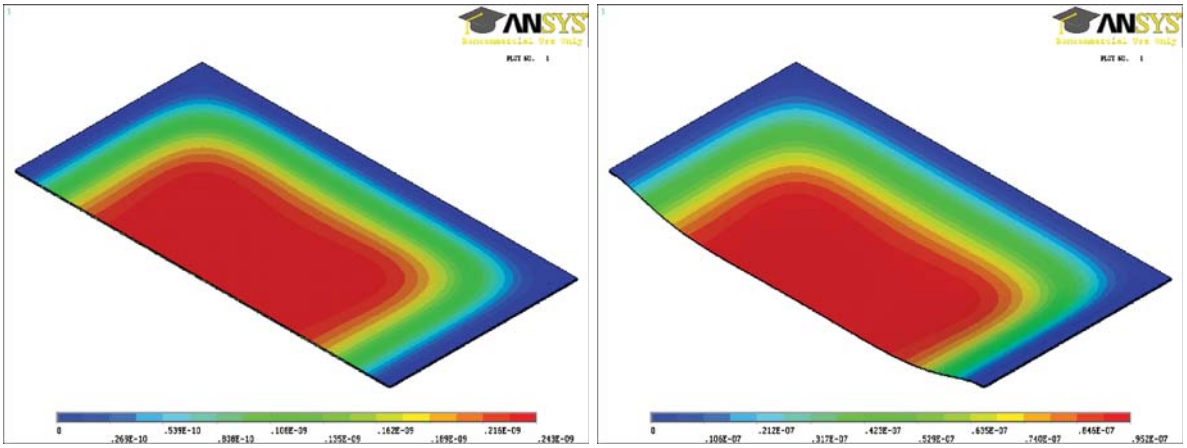

(a) (b)

Figure 6.13. FSI: Microdiaphragm displacement results at the ANSYS side. Simulation results when (a) the microdiaphragm is at the reference position, and (b) the maximum deflection of the microdiaphragm.

increased. This periodic variation in pressure difference case the supply and pumping actions in the valveless micropump. This phenomena is further investigated and verified in following sections.

As was with the initial 3D model, different simulations were carried out to investigate the damping effect caused by the fluid on the microdiaphragm. One analysis carried out a full simulation considering the FSI in the analysis, and another analysis; only considering the electrostatic actuation of the microdiaphragm without the fluid domain. For these simulations, ANSYS based MFX and MFS solvers were used, respectively. The results are presented in Figure 6.15, and the damping effect caused by the fluid is clearly observed.

Since a thin microdiaphragm is simulated during the full 3D model with a narrow air–gap, compared to the initial 3D analysis. Therefore the displacement profile is changed compared to that of Figure 6.8, such that a consistent and flat deflection is achieved in the middle section of the microdiaphragm in full 3D analysis.

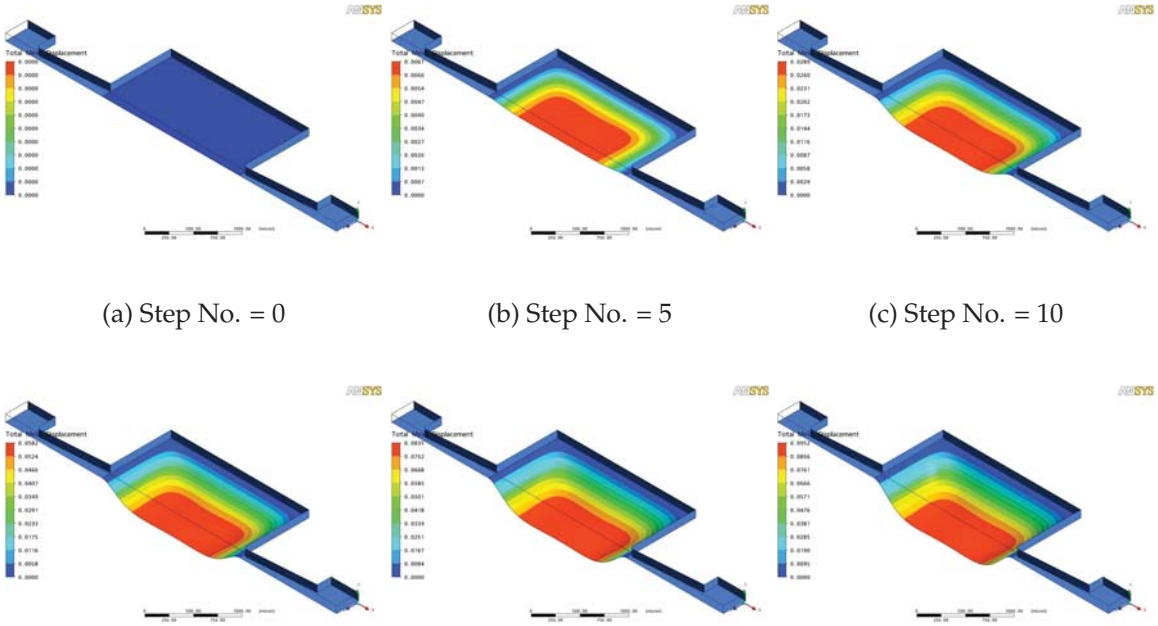

(a) Step No. = 0 (b) Step No. = 5 (c) Step No. = 10

(d) Step No. = 15 (e) Step No. = 20 (f) Step No. = 25

Figure 6.14. FSI: Effect of the microdiaphragm displacement on the fluid region. The Fluid–Solid Interface displacement is synchronised with the microdiaphragm displacement. The complete simulation consist of 200 steps, which relates to 2 $\times T$, where T is the time period of the control signal. Step 25 relates to the first peak of the control signal ($T/4$). As a result of using thin microdiaphragm made of flexible but stable material, the mid section of the microdiaphragm has maintained its flatness. As the amplitude of the control signal is increased, the displacement of the microdiaphragm is also increased and a higher chamber volume is created. As a result the pressure inside the chamber is increased compared to the pressure at the inlet and outlet.

Inlet Flow characteristics During Supply and Pumping Modes

Based on the multi–field CFD results, the inlet flow patterns during the supply mode is presented in Figure 6.16. Generic to all the plots, the laminar flow profile is observed across the inlet neck of the diffuser. Discretised flow velocities at diffuser walls are zero, and the velocity gradually increase towards the center of the cross section of inlet. As the pressure in the chamber is decreased due to the microdiaphragm deflection, more fluid is flowed into the fluidic chamber. The maximum inlet flow rate is reached before the maximum displacement of the microdiaphragm is achieved, hence

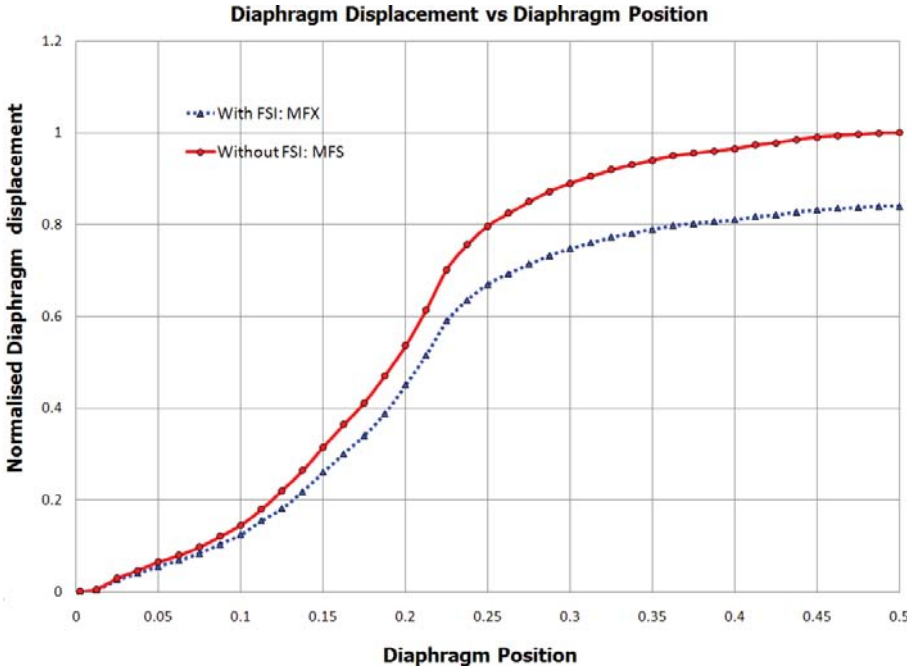

Figure 6.15. Microdiaphragm deformation results for full 3D analysis. Normalised microdiaphragm deformation at the peak input signal (Step No. = 25), along half cross–section of the microdiaphragm, for simulations with and without Fluid–Solid Interaction (FSI). Effects of the fluid damping on the microdiaphragm deflection is clearly noticed. A thin microdiaphragm (5 μm) is simulated during the full 3D model with a narrow air–gap (5 μm), compared to the initial 3D analysis. Therefore the displacement profile is different to that of Figure 6.8, such that a consistent and flat deflection is achieved in the middle section of the microdiaphragm in full 3D analysis.

the relationship between the inlet and outlet velocities, and the velocity of the microdiaphragm (the rate of change in microdiaphragm displacement) is demonstrated.

The inlet flow patterns during the pumping mode is presented in Figure 6.17. As the pressure in chamber is increased due to the reduction in the microdiaphragm deflection (as the control signal amplitude is reduced), fluid is flowed out from the fluidic chamber. The maximum inlet flow rate is reached before the minimum displacement of the microdiaphragm is achieved. Similar to the analogy during supply mode, the relationship between the inlet velocity and the velocity of the microdiaphragm is demonstrated. Additionally, it is noted that the magnitudes of the volume averaged out flow velocities at the inlet during the pumping mode (steps 30–50) are comparatively less than that of the inflow velocities (steps 5 – 25).

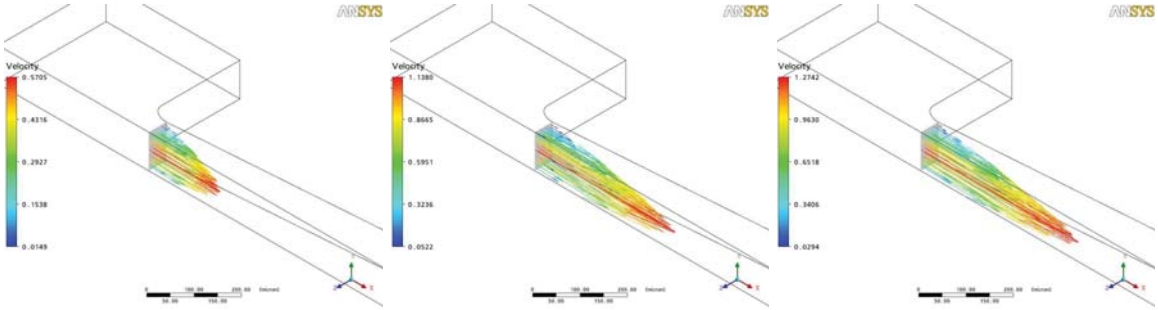

(a) Step No. = 5 (b) Step No. = 10 (c) Step No. = 15

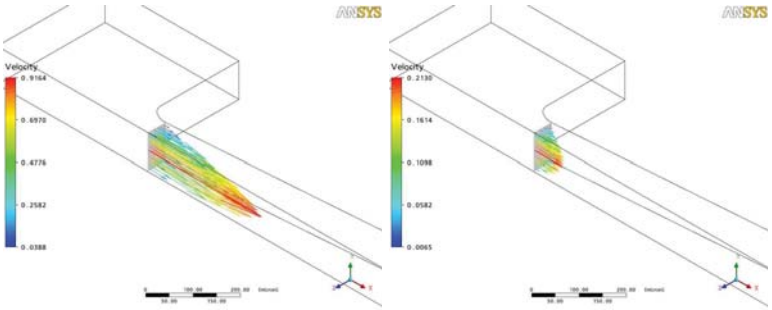

(d) Step No. = 20 (e) Step No. = 25

Figure 6.16. Inlet velocity distribution for various time steps during supply mode. Associated inlet velocities for steps 5 – 25 are shown from (a) – (e) respectively. As the pressure in chamber is decreased due to the microdiaphragm deflection, more fluid is flowed in to the fluidic chamber. The maximum inlet flow rate is reached before the maximum displacement of the microdiaphragm is achieved. This demonstrates the relationship between the inlet velocity and the velocity of the microdiaphragm. Laminar flow characteristics can be identifies at the inlet. For any given step number, maximum flow velocity is observed at the center of the inlet, and zero velocity is observed at diffuser walls.

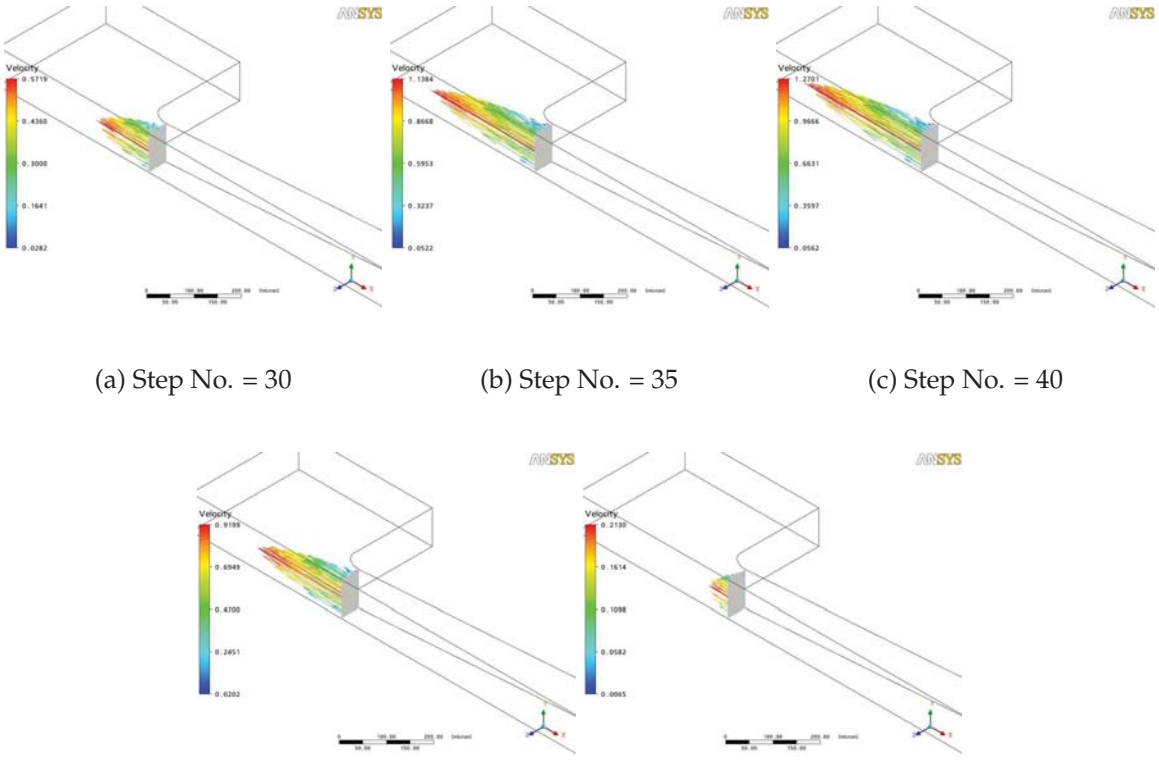

(a) Step No. = 30 (b) Step No. = 35 (c) Step No. = 40

(d) Step No. = 45 (e) Step No. = 50

Figure 6.17. Inlet velocity distribution for various time steps during pumping mode. Associated inlet velocities for steps 30 – 50 are shown from (a) – (e) respectively. As the pressure in chamber is increased due to the reducing microdiaphragm deflection (as the control signal amplitude is reduced), fluid is flowed out from the fluidic chamber. The maximum inlet flow rate is reached before the minimum displacement of the microdiaphragm is achieved. This demonstrates the relationship between the inlet velocity and the velocity of the microdiaphragm, similar to Figure 6.16. The magnitude of the out flow velocities (steps 30–50)are comparatively less than that of the inflow velocities (steps 5 – 25 in Figure 6.16).

Outlet Flow characteristics During Supply and Pumping Modes

The multi–field results based flow behaviour at the outlet is elaborated in this section. The outlet flow patterns during the supply mode is presented in Figure 6.18. Similar to the inlet flow characteristics, the laminar flow profile is observed across the outlet neck of the diffuser. As the pressure inside the chamber is decreased due to the micro-diaphragm deflection, fluid is flowed in to the fluidic chamber through the outlet as well. However, in comparison , the magnitudes of the volume averaged flow velocities at the inlet are higher than that of the outlet; resulting in a net flow in to the chamber through the inlet, during the supply mode.

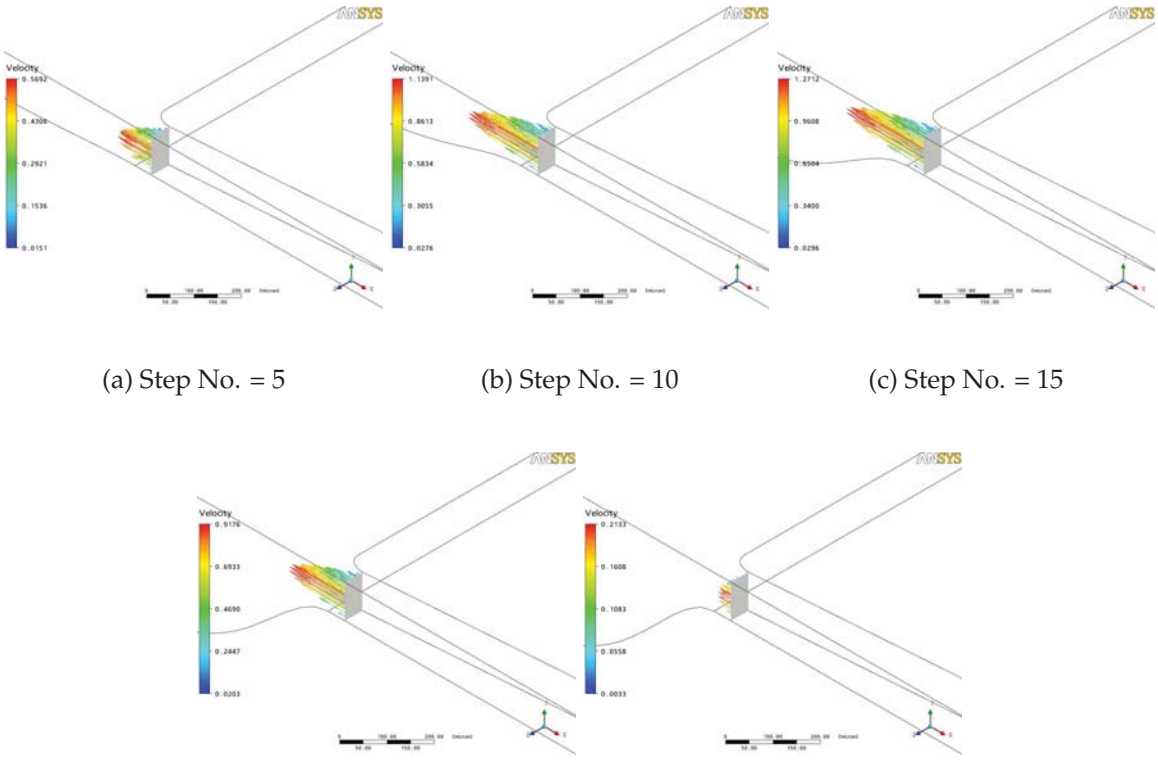

(a) Step No. = 5 (b) Step No. = 10 (c) Step No. = 15

(d) Step No. = 20 (e) Step No. = 25

Figure 6.18. Outlet velocity distribution at the outlet neck, for various time steps during supply mode. Associated inlet velocities for steps 5 – 25 are shown from (a) – (e) respectively. As the pressure in chamber is decreased due to the microdiaphragm deflection, fluid is flowed into the fluidic chamber through the outlet as well. In comparison with Figure 6.16, the magnitudes of the flow rates at the inlet are higher than that of the outlet; resulting in a net flow into the chamber through the inlet, during the supply mode.

The inlet flow patterns during the pumping mode is presented in Figure 6.19. As the pressure in chamber is increased due to the reducing microdiaphragm deflection (as the control signal amplitude is reduced), fluid is flowed out from the fluidic chamber, through the outlet as well. The maximum inlet flow rate is reached before the minimum displacement of the microdiaphragm is achieved.

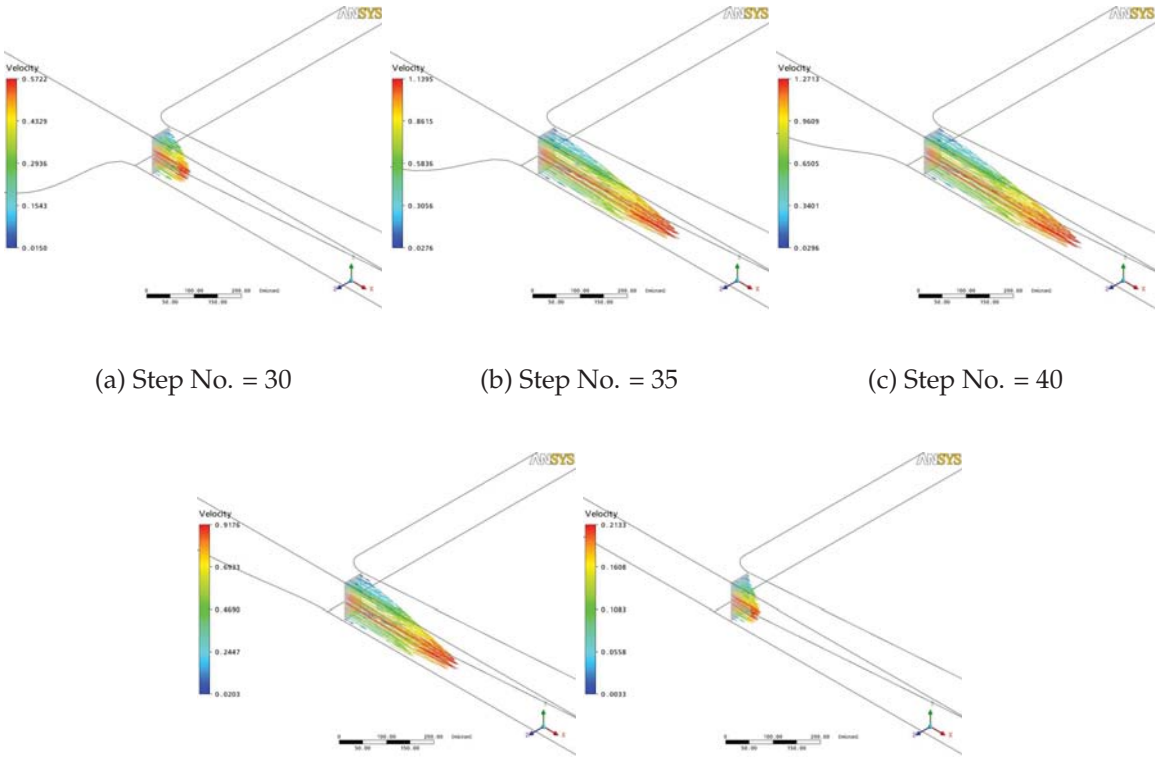

(a) Step No. = 30 (b) Step No. = 35 (c) Step No. = 40

(d) Step No. = 45 (e) Step No. = 50

Figure 6.19. Outlet velocity distribution for various time steps during pumping mode. Associated outlet velocities for steps 30 – 50 are shown from (a) – (e) respectively. As the pressure in chamber is increased due to the reducing microdiaphragm deflection, fluid is flowed out from the fluidic chamber through the outlet as well. In comparison with Figure 6.17, the magnitudes of the flow rates at the outlet are higher than that of the inlet; resulting in a net flow out from the chamber through the outlet, during the pumping mode.

It is noted that in comparison, during the pumping mode, the magnitudes of the volume averaged flow velocities at the outlet are higher than that of the inlet; resulting in a net flow out from the chamber through the outlet. Furthermore, the magnitudes of the volume averaged out flow velocities at the outlet during the pumping mode (steps

30–50) are comparatively higher than the volume averaged inflow velocities during the supply mode (steps 5 – 25). These results are further summarised and presented in Figure 6.20. It should be noted that a 10 Hz AC sinusoidal signal with 10 V peak–to–peak amplitude was used for the simulation results presented in Figures 6.20 and 6.21.

Overall Flow Rate Analysis of the Micropump

Based on the FEA based multi-field CFD simulations, the volume–averaged flow velocity at the inlet and the outlet are compared for the derivation of the overall flow rate of the micropump. As was introduced in Chapter 5, the volume–averaged velocity $\overline{v}$ is defined as (White 1999)

$$\overline{v} = \frac{1}{A} \int_A u_a \, dA, \tag{6.5}$$

for axial velocity u_a across a cross–section of a diffuser. In relation to the simulated micropump model, A is defined to be the cross–sectional area of the inlet and outlet diffuser necks.

Once the volume averaged velocities are calculated, the flow velocity is plotted against the time steps in Figure 6.20 (a), for both inlet and the outlet. During the supply mode, the volume averaged flow rates at the inlet are always higher than that at the outlet. Similarity, during the pumping mode, the volume averaged flow rates at the outlet are higher than the inlet. A positive rate indicates that fluid is flowing in the chamber, whereas a negative rate indicates fluid is flowing out of the chamber.

Additionally, the net flow rate plot with respect to the pumping chamber is depicted in Figure 6.20 (b). As can be seen from this figure, during supply mode, more fluid flows into the chamber through inlet than outlet. Whereas, during pumping mode, more fluid flow out from the outlet than inlet. These results clearly demonstrate the pumping effect of the SAW device based valveless micropump. As is mentioned before, due to the quadratic relationship between the control signal and the electrostatic actuation force, the vibration frequency of the microdiaphragm is twice of the input signal frequency. Therefore, for one period of the control signal (T or 100 steps), two full cycles of vibrations are observed at the microdiaphragm, hence two full cycles of flow rate variations are observed. Therefore, the simulation based average flow rate (Q_{avg}) of the micropump can be calculated as

$$Q_{avg} = \frac{2}{T} \int_0^{T/4} Q(t) \, dt, \tag{6.6}$$

where T is the time period of the control signal and $Q(t)$ is the instantaneous volume averaged flow rate which can be calculated as $Q(t) = A_1\overline{v}$.

Based on Equations 6.5– 6.6, and CFD results of the micropump, the average flow rate of the designed micropump at 10 Hz control frequency is calculated to be 43 μl per minute. Such flow rates under low–powered actuation indicates competitive performance characteristics, compared to the other reported analysis on valveless micropumps (Yao *et al.* 2007, Nisar *et al.* 2008d). Further to this point, it should be noted that based on the published research, most of the valveless micropump models utilise high

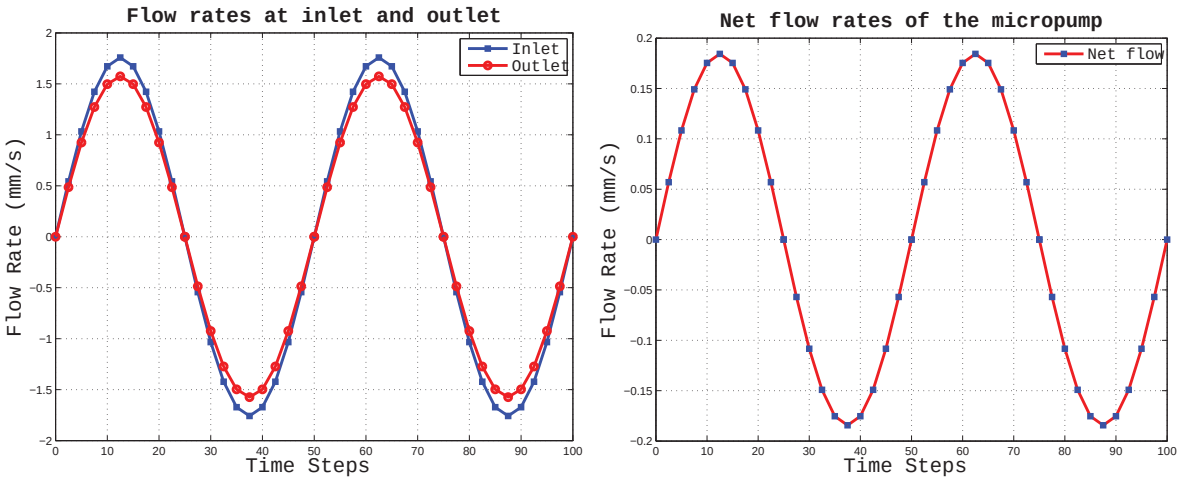

(a) (b)

Figure 6.20. Averaged flow velocities at inlet and outlet, and averaged net flow velocities for the full 3D model of the micropump. (a) During the supply mode, the volume averaged flow rates at the inlet are always higher than that at the outlet. Similarity, during the pumping mode, the volume averaged flow rates at the outlet are higher than the inlet. (b) Demonstrates the net fluid flow behavior in and out of the microfluidic chamber. During supply mode, more fluid flows in to the chamber through inlet than outlet. Whereas, during supply mode, more fluid flow out from the outlet than inlet. These results clearly demonstrate the pumping effect of the SAW device based valveless micropump. Due to the quadratic relationship between the control signal and the electrostatic actuation force, the vibrating frequency of the microdiaphragm is twice of the input signal frequency. Therefore, for one period of the control signal (T or 100 steps), two full cycles of vibrations are observed at the microdiaphragm, hence two full cycles of flow rate variations are observed.

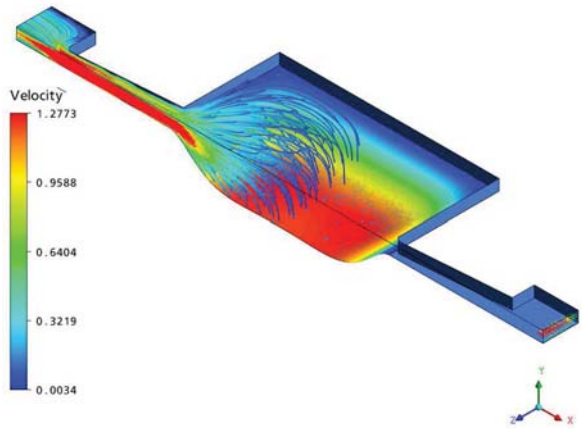

(a) Inlet flow at $t = T/8$

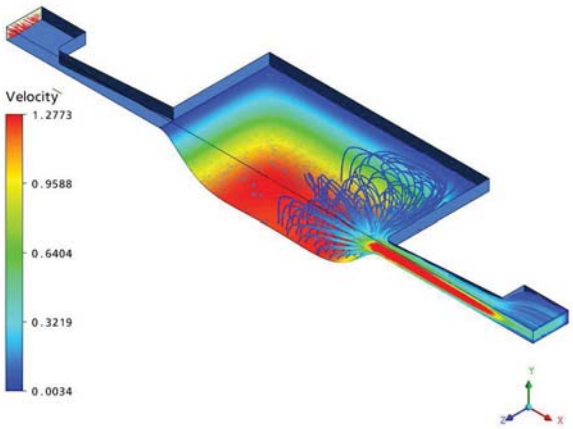

(b) Outlet flow at $t = T/8$

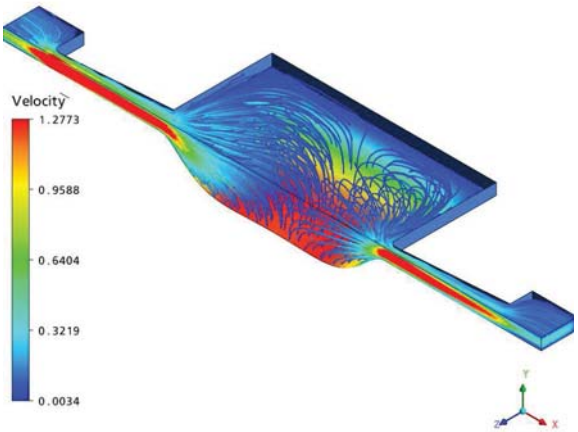

(c) Combined flow at $t = T/8$

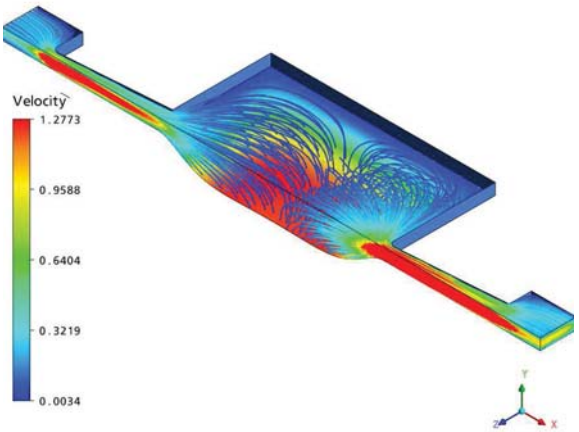

(d) Combined flow at $t = 3T/8$

Figure 6.21. The 3D micropump velocity profiles at the inlet and outlet, and overall flow behaviour at two different states of operation. The inlet fluid flow is synchronised with the Fluid-Solid Interface displacement (the diaphragm displacement). (a) Inlet flow pattern during supply mode $t = T/8$, where T is the time period of the control signal. (b) Outlet flow patter during the same instant in supply mode $t = T/8$. (c) Combined flow patterns for both inlet and outlet during an instance of supply mode $t = T/8$. During the supply mode, more fluid flows in to the pumping chamber at the inlet, compared to that at the outlet. (d) Combined flow patterns for both inlet and outlet during an instance of pumping mode $t = 3T/8$. During the pumping mode, more fluid flows out from the pumping chamber at the outlet, compared to that at the inlet.

actuation voltages (Nguyen *et al.* 2002, Squires and Quake 2005, Tsai and Sue 2007, Yao *et al.* 2007, Nisar *et al.* 2008d). Therefore, the developed valveless micropump presented in this chapter, especially with low–powered and wireless interrogation is of high suitability for a host of biomedical and other applications, as was discussed in Chapters 1 and 2.

The overall flow behaviour of the micropump is summarised in Figure 6.21. Here, a combination of inlet and outlet streamlines, along with the deflected interface are depicted to highlight the velocity variation of the fluid flow. Figures 6.21 (a) and (b) represent the inlet and outlet flow patterns for an instance in supply mode ($t = T/8$), respectively. Whereas Figure 6.21 (c) represents the combined flow pattern for the same instance in supply mode ($t = T/8$). Furthermore, Figure 6.21 (d) represents a combined inlet and outlet flow pattern for an instance in pumping mode ($t = 3T/8$).

6.9 Further Device Developments

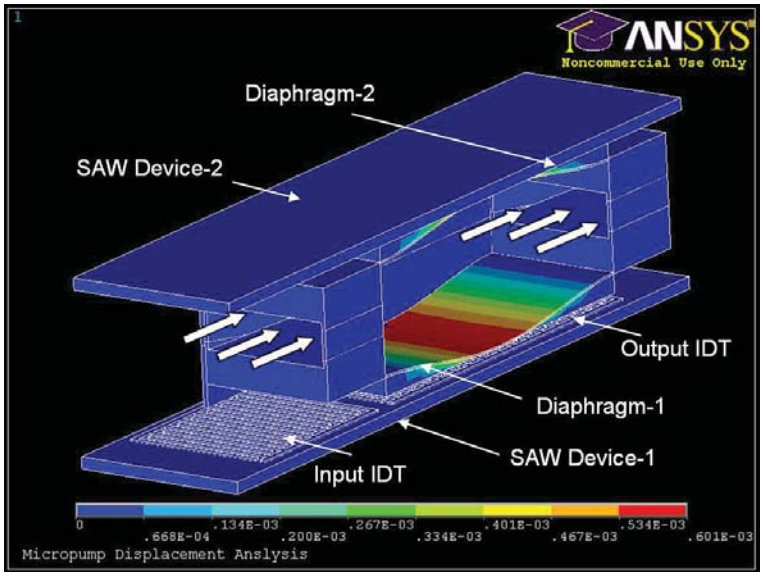

Figure 6.22. A micropump structure based on two SAW devices. A sectional 3D view of a micropump structure with two SAW devices and two diaphragms that cab ne implemented to pump fluid/drug at higher flow rates, utlising the same interrogating signal.

After successful FEA based CFD modelling of the SAW based electrostatically actuated micropump, the potential for further device developments can be identified. In order to increase the pumping effect and gain higher flow rates at low power, the proposed

design can be further extended by incorporating two SAW devices and two microdiaphragms as shown in Figure 6.22. This way, the device can be controlled by utilising the same interrogating RF signal for both the SAW devices.

Due to the presence of two actuators in either side of the microfluidic chamber that are controlled by two SAW devices, the device would be capable of modulating the fluid flow with increased force and accuracy, as the device can absorb more power from the same interrogating RF signal, through the two SAW devices. Such a model could also ease the device fabrication, due to its symmetry.

6.10 Chapter Summary

In this chapter, novel investigation methodology is presented to model and analyse 3D micropump structures with complex coupling effects. FEA based multi–field analysis is developed and carried out in performing detailed CFD analysis of the device, thereby a more realistic modelling of the device was facilitated. The Fluid–Solid Interfaces (FSIs) of the device is effectively modelled and the pumping effect is clearly demonstrated. Both preliminary and detailed 3D modelling results were presented, The ability to operate such a micropump using comparatively low voltages was clearly demonstrated.

The results of this research have lead to the identification of important areas for further improvement of the micropump performance under low–power operation. In total drug delivery systems, some of the important design characteristics for the delivery of substances to the body are accuracy, resolution, safety and control. Therefore additional features on such micropumps would be integrated–pressure sensors, integrated–flow restrictors and fluid filters. Therefore analysis of micropump performance at an integrated level is of high importance, and are considered to be some of such areas to be investigated in future.

Additionally as a result of this newly presented dual interaction analysis, development of microfluidic devices for host of other applications can be carried out. As a result of such numerical modelling and analysis of micro devices at pre fabrication stage, success rates of fabrication could be improved and the device cost could be reduced, in addition to the efficient optimisation of device parameters.

Chapter 7

Conclusions and Future Directions

THIS Chapter draws together the conclusions from the work undertaken in this research, and recommends directions for future research. Furthermore, a summary of original contributions is also presented, and some concluding remarks are highlighted.

7.1 Introduction

In this research an attempt was made to design and develop remotely interrogated, implantable micropump for applications such as drug delivery. In addition to proposing a novel interrogation mechanism, the emphasis in this thesis was on the development of computational modelling based on FEA and CFD numerical methods.

Based on the review carried out in Chapter 1, it was realised that the number of patients suffering from life threatening global health problems and chronic diseases such as cardiovascular deceases (hypertension, heart attack, stroke), septicaemia, cancer, diabetes, melancholia, and malignant lymphoma have increased more than ever before.

It was further noted that conventional drug delivery methods such as oral tablets or injections consist of limitations such as variable absorption profile, need of frequent dosing, and ineffectiveness in site specific delivery of drugs. Some clinical situations, however, necessitate either an external control of the drug delivery rate, or a volume of drug that is beyond the capabilities of existing controlled-release formulations. Implantable drug delivery pumps have been devised to meet these situations.

Furthermore, an extensive review has been carried out in Chapter 2, on micropumps, microvalves, and SAW based wireless communication for RF-MEMS and Bio-MEMS applications. Based on this fruitful information, it was concluded that overall commercialisation of rapidly growing, MEMS micropumps in total drug delivery systems and other biomedical applications is still in its beginning.

A vast amount of technical information was noted and discussed for a number of micropump concepts. However, based on the review it was further highlighted that most of the reported novel micropumps for drug delivery applications still need to be incorporated onto practical devices.

To address these issues, a wirelessly operated, securely actuated, fully passive micropump was proposed and designed using a novel method, which is based on surface acoustic wave (SAW) devices and wireless transcutaneous radio frequency (RF) communication. The device is capable of extracting the required power from the RF signal itself, and hence the need for a battery and active electronics was successfully negated. Moreover, a SAW correlator was used for secure interrogation of the device, where the device responds only to a unique RF signal, which has the same code as was implanted in the SAW correlator.

The design and development of the micropump, and its microfluidic analysis was carried out using industry standard modelling and simulation tools. A strong emphasis has been given on utilising CFD to analyse the microfluidic flow behaviour of the device, and FSI analysis has been performed simultaneously on the micropump. In order to make the fabrication process easier, the micropump was designed to be valveless; consisting of diffuser elements for flow rectification.

7.2 Thesis Conclusions

In this section, a summary and conclusions are made based on the research carried out in this dissertation.

As mentioned in Section 7.1, Chapter 1 introduced the the significance in developing novel MEMS based micro drug delivery systems for implantable biomedical applications. Important limitations in current systems were highlighted, and questions were raised regarding the significance of modelling and developing wireless implantable drug delivery systems for various life threatening disorders. As such; (i) the suitability of the existing micropumps technology for implantable drug delivery, (ii) strength of existing technology to develop low cost and reliable micropumps, (iii) possibility of developing remote low–powered, transcutaneous interrogation systems, (iv) the need and the possibility to incorporate a secure operation, by providing a great protection against spurious RF signals, (v) possibility to develop a fully passive device with no active electronics, (vi) techniques that could be used for modelling and analysis of complex microstructures, at modular levels as well as integrated system level, and (vii) possibility and requirement to carry out advance FSI analysis for 3D models of MEMS micropumps, incorporating interactions between multiple physics fields, are some of the critical questions raised in Chapter 1.

Chapter 2 provided a comprehensive review of micropumps, their actuation mechanisms, and microvalves that form an integral part of micro drug delivery devices and systems. Main advantages and disadvantages associated with different types of micropump actuation mechanisms were discussed. Moreover, their critical design and performance parameters such as size, mass, actuation voltage, power requirements, and flow rates were reviewed. The important features associated with static–geometry based, passive, diffuser/nozzle elements found to be an attractive, low cost solution for flow rectification. Furthermore, Chapter 2 provided a discussion on SAW device based

wireless communication capabilities, in view of their suitability for low–powered implants. Importantly, the novel, wireless and batteryless, and secure interrogation mechanism for biomedical implants was introduced and described in Chapter 2, which was then implemented in Chapters 3, 4 and 6.

In Chapter 3 the novel SAW based actuation mechanism was implemented to generate low–powered microactuations. A detailed theoretical analysis was presented, explaining SAW device based actuator operation, and ANSYS based FEA simulations were carried out and results were presented and analysed for the SAW actuator model.

Static analysis results were generated and validated against the theoretical model developed using Rayleigh–Ritz method. Subject to design simplifications in the analytical model, a good correlation was observed between the theoretical and simulated displacement curves.

Once the static analysis was completed, transient analysis was carried out in order to study the dynamic behaviour of the SAW device based electrostatic actuator. This was substantial in investigating the operating frequency of the conductive plate, and based on the simulations, it was found that the operating frequency of the actuator is much less than that of the SAW frequency. Furthermore, an effective mechanism was discovered and presented as some potential future work, which could be used to design ultrasonic micropumps with better isolation. This is further discussed in Section 7.3.

In Chapter 4, the SAW based interrogation mechanism was further extended to analyse the performance of a microdiaphragm, as a critical and essential component of the proposed micropump structure. Important characteristics of a corrugated microdiaphragm were investigated, as an effective mechanism to improve low–powered microdeflections. As an extended analysis from Chapter 3, ANSYS based FEM was performed to evaluate the performance of corrugated microdiaphragms, and the dependency of the performance on different corrugation types, corrugation parameters, material properties, and design practices were also investigated.

FEA based static results were validated using Rayleigh-Ritz method based extended analytical model. The significance of FEA to simulate and analyse complex scenarios with complex geometries was highlighted as an alternative option to analytical modelling, in the context of structural analysis of corrugated microdiaphragms. Based on the computational modelling results, a corrugated microdiaphragm made of polyimide based sinusoidal corrugations and a square–shaped diaphragm, was able to

generate more deflections compared to a flat diaphragm. Additionally, a fabricated flat microdiaphragm structure was tested using limited facilities, mainly to verify the electrostatic actuation concept. It was highlighted that with the availability of better fabrication facilities, a corrugated microdiaphragm could be fabricated for a better representation and realisation of the simulated model. This is further discussed in Section 7.3.

Chapter 5 in this thesis concentrated on accurate and effective modelling of micro diffuser/nozzle elements as a flow rectification mechanism for microfluidic devices and systems. Detailed 2D and 3D analysis were performed and results were presented in relation to flat–walled diffusers highlighting their flow rectification capability at low Reynolds numbers and laminar flow conditions. FEA based CFD analysis were carried out using ANSYS tools, to investigate the relationship between dimensions and the performance, and to highlight the importance in parameter optimisation. The results from the numerical analysis were quantified in terms of pressure loss coefficient, by calculating the diffuser efficiency for 3D diffuser elements.

The general trend associated with the variation of pressure loss coefficient with diffuser angle was found to be similar to that for high Reynolds number turbulent flow. However, unlike at high Reynolds numbers, it was found that pressure loss coefficients at low Reynolds numbers vary significantly with Reynolds number. It was also observed that trends of variation in the pressure loss coefficient with Reynolds number are different for small and large diffuser angles. Contrary to past claims, flow rectification was shown to be indeed possible for laminar flows with low Reynolds numbers.

In Chapter 6, 3D multi–field modelling and analysis of a valveless, SAW based micropump was investigated and some important findings were presented. Advanced FSI analysis of the 3D micropump structure was carried out, for the first time, utilising FEA based CFD techniques, and the interaction between fluid, solid, and electrostatic fields were analysed simultaneously. ANSYS and CFX based advanced techniques were implemented to effectively model the FSIs of the micropump, and the pumping effect was clearly demonstrated.

Both preliminary and detailed 3D modelling results were presented, and the low–powered operation of the micropump was demonstrated, in view of implementing such a device for *in–vivo* applications to allow nanoliter drug delivery.

Results and new findings in this research had lead to the identification of important areas for further improvement of the micropump performance under low–powered operation.

7.3 Recommendations for Future Work

7.3.1 Further Computational Modelling

In total drug delivery systems, some of the important design characteristics for the delivery of substances to the body are accuracy, resolution, safety and control. Therefore additional features on such micropumps would be, integrated–pressure sensors, integrated–flow restrictors, and fluid filters. Therefore analysis of micropump performance at an integrated level is of high importance, and can be highlight as potential future research areas in this field.

Additionally, the new contributions made in regard to multi–field analysis with interactions between multiple physics fields, can be further utilised to develop FEA based CFD models of microfluidic devices for host of other applications such as Lab–on–a–Chip (LoC), and micromixing.

Furthermore, advance CFD analysis can be carried out at the design stage, for various types of drug, incorporating interactions between Non-Newtonian domains such as blood. As a result of such numerical modelling and analysis of micro devices at pre fabrication stage, success rates of fabrication can be improved at low cost due to less repetitions.

7.3.2 Smart Drug Delivery System with SAW based Sensing

It would be highly desirable to combine a micro drug delivery device with a totally implanted sensory system, thereby achieving the development of a completely *close-loop* smart drug delivery systems for advance performance, with no human interference.

The proposed SAW based micropump device could be further improved by integrated passive smart sensing mechanisms such as, pressure sensing for hypertension, glucose sensing for diabetes, rigidity sensing of a mammalian cells for cancer screening. The

attractive feature is that the SAW based sensors technology is a well established research field, and therefore the same SAW based communication technique could be incorporated for the development of implantable smart devices.

7.3.3 Considerations in Implementing Transcutaneous Systems

It is critical that an implantable micropump must be biocompatible and safe and accurate in all aspects. In incorporating a drug reservoir to a drug delivery system, extra care is needed to avoid the danger of *dose dumping* [2], even though it is not a common failure mechanism in drug delivery implants (Ranade and Hollinger 2004). Overdosing, on the other hand is not considered to be as easily correctable, and in some situations delivering less amount of a drug on the prescribed schedule can be considered dangerous as well (Tsai and Sue 2007, Ranade and Hollinger 2004). Therefore, extensive testing and verification of micropumps, and total delivery systems is a must in these critical implants.

Issues such as splitting the tubing in mechanical micropumps, mechanical and electrical failure in the actuation mechanism, and piercing the reservoir due to mechanical trauma could directly cause overdosing, and hence rigorous testing and verification are needed at all stages of the product life cycle to avoid such failures.

In addition to aforementioned issues, the viability of transcutaneous energy transfer methods in different conditions, easy programmability, location of the implant, effective sterilisation of the device, and easy administration are also important aspects to be further investigated.

The accuracy and precision of delivery must be maintained over an extended period of time. To justify the surgery associated with the implant, this period must be at least 2 years or preferably 5 years (Ranade and Hollinger 2004). Furthermore, the sufficient biological, physical, and chemical stability and compatibility of the drug within the pump is also required.

[2] Dose dumping is a phenomenon of drug metabolism in which environmental factors can cause the premature and exaggerated release of a drug. This can greatly increase the concentration of a drug in the body and thereby produce adverse effects or even drug-induced toxicity (Ranade and Hollinger 2004)

7.4 Summary of Original Contributions

The original contributions of this thesis are summarised in this section. The goal of this thesis was to present several significant and novel contributions to the modelling and simulation of MEMS based wireless microactuators and micropumps, microfluidic flow analysis based device optimisation, and advanced computational techniques for Fluid–Structure Interaction (FSI) of coupled–fields. These research contributions are:

- **A Novel Wireless and Secure Interrogation Mechanism:** A novel batteryless and low–powered, secure, and wireless interrogation mechanism for implantable MEMS devices was introduced and investigated. This approach is based on SAW technology and significantly different from currently existing techniques, as the proposed method consists of dual functionality; the interrogation and actuation.

- **A Novel SAW based Wireless and Low–Powered Microactuator:** A new SAW based wireless microactuator is investigated. A theoretical model of the actuation mechanism is developed, based on the underlying theory on SAW propagation in a piezoelectric media, and electrostatic actuation. Furthermore, the proposed actuator model was implemented and analysed utilising ANSYS based FEA techniques, and results were verified using analytical models.

- **New Combinations and Effective Techniques for Optimisation of Low–Powered Microdiaphragm Performance:** New combinations of attractive methodologies were investigated and developed to optimise the performance of microdiaphragms for low–powered microdisplacements. To improve the microdisplacements of low profiled microdiaphragms, analysis of the effect of various corrugation profiles on diaphragm performance was presented and FEA based coupled–field analysis techniques was implemented, and various effective approaches were suggested and investigated to enhance the flexibility and stability of low profiled microdiaphragms.

- **A Novel FEA based CFD Analysis of Diffusers under Low Reynolds Number, Laminar Flow Conditions:** Design, analyse and optimisation of diffuser/nozzle based, valveless flow rectification mechanisms for microfluidic devices were presented. As a new contribution, FEA based CFD analysis was utilised to investigate the flow rectification phenomena in 2D and 3D flat–walled diffuser elements,

for low Reynolds number and laminar flow conditions. This represents an extension to the currently published research on diffuser flow analysis at the design stage, as the analysis that was carried out in this research provides a qualitative and quantitative relationship between diffuser efficiency and Reynolds numbers.

- **A Novel Methodology for Advanced Analysis of Micropumps with 3D Multi–Field Interactions:** A novel approach was presented in developing advanced modelling and analysis capabilities for low-powered micropumps, especially for an implantable, batteryless, fully passive device that is aimed at micro drug delivery applications. The new 3D modelling and simulation methodology is a combination of 3D multi-field analysis, and multiple code coupling capabilities in commercially available modelling and simulation tools. Both ANSYS based FEA code, and CFX based CFD code have been simultaneously combined during the proposed multi–field analysis to simulate the functionality and the flow behaviour of SAW based electrostatically actuated valveless micropump. This Fluid-Solid Interactions (FSIs) between multiple physics fields is effectively modelled and investigated for both preliminary and fully detailed 3D models of a diffuser/ nozzle based micropump.

7.5 Closing Comments

This thesis presented a number of novel contributions that demonstrated the modelling and analysis of microactuators, microdiaphragms, microdiffusers and micropumps for potential biomedical applications. Furthermore, this thesis investigated the operation of such wirelessly controlled micropump for drug delivery applications, without the need for implanted power source and active electronic circuitry. New contributions were also made in the area of FEA and CFD modeling of low-powered microstructures. By carrying out state of the art research in this kind, this thesis has facilitated the addition of new contributions to the fields such as wireless communication, biocompatible microfluidic device analysis, implantable device development and implementation.